PDE Methods for Nonlocal Models[*]

Carlo R. Laing[†] and William C. Troy[‡]

Abstract. We develop partial differential equation (PDE) methods to study the dynamics of pattern formation in partial integro-differential equations (PIDEs) defined on a spatially extended domain. Our primary focus is on scalar equations in two spatial dimensions. These models arise in a variety of neuronal modeling problems and also occur in material science. We first derive a PDE which is equivalent to the PIDE. We then find circularly symmetric solutions of the resultant PDE; the linearization of the PDE around these solutions provides a criterion for their stability. When a solution is unstable, our analysis predicts the exact number of peaks that form to comprise a multipeak solution of the full PDE. We illustrate our results with specific numerical examples and discuss other systems for which this technique can be used.

Key words. pattern formation, integro-differential equation, PDE, nonlocal

AMS subject classifications. 34B15, 34C23, 93C15, 34C11

DOI. 10.1137/030600040

1. Introduction. Pattern formation in neuronal networks is an area of ongoing interest [10, 11, 12, 13, 19, 26, 31, 35, 37, 40, 42, 43, 53, 54, 59, 60, 65]. In this paper, we investigate spatially localized regions of high activity, often referred to as "bumps." These are of interest in modeling working memory, the ability to remember information over a time-scale of a few seconds [18, 40, 63, 66]. Experiments on primates show that there exist regions of neurons that have elevated firing rates during the period that the animal is "remembering" some aspect of an object or event [17, 29, 45]. These regions are spatially localized in a location determined by the relevant aspect of the object or event being remembered. Further applications of pattern formation in neural systems include head-direction systems [58, 67], where a constantly updated bump of activity represents the current heading of an animal, and feature selectivity in the visual cortex [12, 13, 37], where bump formation may be related to the "tuning" of a particular neuron's response. Similar models to those studied here have been used to model the "look, plan, reach, remember" dynamics in the perseverative reaching of infants and their longer term cognitive development [60]. Also, in a recent book, Giese [31] uses systems of the form (1.1) to study problems related to visual perception of motion, the planning of eye movements, and robot navigation.

Realistic models for these types of activity involve spatially extended systems of coupled neural elements and the study of localized areas of high activity in these systems. Previous studies have focused on nonlocal rate models [1, 2, 3, 10, 11, 12, 13, 31, 37, 42, 53, 54, 66],

[†]Institute of Information and Mathematical Sciences, Massey University, Private Bag 102-904, North Shore Mail Centre, Auckland, New Zealand (c.r.laing@massey.ac.nz).
[‡]Department of Mathematics, University of Pittsburgh, Pittsburgh, PA 15260 (troy@math.pitt.edu).

in which a neural element is described by a scalar variable (e.g., a firing rate), and more complicated "spiking neuron" models [18, 35, 40, 63], which take into account the intrinsic dynamics of single neurons. We concentrate here on rate models exclusively.

In this paper, our goal is to develop PDE methods to analyze the dynamics of localized pattern formation in rate models of the form

$$(1.1) \qquad \frac{\partial u(x,y,t)}{\partial t} = -u(x,y,t) + \iint_\Omega w(x-q, y-s) f(u(q,s,t) - th) \, dq \, ds,$$

where $\Omega \subset \mathrm{R}^2$. In the context of the neuronal models discussed above, $u(x,y,t)$ represents the synaptic input to a neuron at position $(x,y) \in \Omega$ at time t, w denotes the connectivity, or coupling, between neural elements, $f(u(x,y,t) - th)$ is the firing rate of the neuron at the position (x,y), and th is the threshold of excitation. Equations of the form (1.1) and its one-dimensional analogue have been used extensively in neural modeling [11, 12, 13, 26, 31, 37, 40, 43, 59, 65]. However, most of the previous attention has been focused on the one-dimensional analogue of (1.1):

$$(1.2) \qquad \frac{\partial u(x,t)}{\partial t} = -u(x,t) + \int_\Omega w(x-y) f(u(y,t) - th) \, dy.$$

Because of the lower dimensionality of this system, it is easier to study than (1.1), and for applications such as the head-direction system and feature selectivity in the visual system this one-dimensional system may be appropriate, since the independent variable x corresponds to a one-dimensional quantity, an angle. However, the cortex is an essentially two-dimensional sheet, and thus (1.1) is a more realistic model for pattern formation in a neuronal system.

Little analytical work has been done on (1.1). Specifically, there are results relating to circularly symmetric solutions [59, 65], for which the two-dimensional problem is effectively reduced to a one-dimensional one. There has also been some very recent work on a "two layer" analogue of (1.1), where the activity of two populations of neurons are modeled [25]. However, these authors primarily studied target patterns, which also have circular symmetry. Also, Bressloff et al. have studied (1.1) on a sphere [12] and have also considered this equation when there is a lattice of inhomogeneities in the domain, using the symmetry of this lattice to determine the types of solution that can occur [11, 13].

Equations similar to (1.1) and (1.2) also occur in material science [5, 6, 7, 8, 16, 27, 28]. An often-studied equation is

$$(1.3) \qquad \frac{\partial u(x,t)}{\partial t} = -ju + f(u) + \int_{-\infty}^{\infty} w(x-y) u(y,t) \, dy,$$

where $j = \int_{-\infty}^{\infty} w(x) \, dx$, w represents nonlocal interactions, and f typically has three zeros. Physically important solutions include heteroclinic, homoclinic, and periodic orbits. Solutions remain continuous when the function $g(u) \equiv ju - f(u)$ is monotonic. In this case, the equation $v = g(u)$ can be inverted to give $u = h(v) \equiv g^{-1}(v)$, and (1.3) becomes

$$(1.4) \qquad h'(v) \frac{\partial v(x,t)}{\partial t} = -v(x,t) + \int_{-\infty}^{\infty} w(x-y) h(v(y,t)) \, dy.$$

The similarities between (1.4) and its two-dimensional generalization, and (1.2) and (1.1), suggest that many of the results presented here will also be applicable to those models.

Our main focus will be on the two-dimensional model (1.1). We will develop techniques which describe how families of multibump solutions form when the coupling function $w(x,y)$ is a function of distance in R^2 only, i.e.,

$$(1.5) \qquad w(x,y) = w\left(\sqrt{x^2 + y^2}\right).$$

Solutions of (1.1) are translationally invariant when (1.5) holds.

Our approach is twofold: first, we develop a method to derive a fourth order PDE which is equivalent to the integral equation. To our knowledge an equivalent PDE for the two-dimensional problem has not previously been derived. Second, we will analyze the PDE and develop techniques which show how families of peaks form when circularly symmetric steady states of (1.1) are unstable.

We hope that the insights obtained by considering coupling functions satisfying (1.5) will provide a basis for extensions to more complicated settings. For example, in the cortex it is important to consider connectivity functions that incorporate the "patchy" nature of neural connections [9, 34, 44], which break the translational invariance of the system. As mentioned above, Bressloff et al. have studied this effect [11, 13].

One assumption in studying (1.1) and (1.2) is that the behavior of neurons can be characterized by their firing rate alone and, more importantly, that excitatory and inhibitory neurons can be represented by a single population with a connectivity function that takes both positive and negative values. A more realistic approach would involve two variables, representing the activities of the excitatory and inhibitory populations, and coupling functions between and within the populations that are nonnegative. Although our models are less realistic in the sense that we use only one population, lumping the excitatory and inhibitory neurons together, they have the advantage of involving only one variable.

Note that we are not addressing the processes involved in the formation of the connectivities represented by $w(x)$ but are instead interested in the possible patterns of neural activity that can exist in the system once these connectivities are in place.

Overview. In the next section, we summarize previous results for one-dimensional models. The insights obtained in the study of the one-dimensional case play an important role in section 3, where we study two-dimensional models. Section 3 begins with numerical results which show the types of multibump solutions that can arise for specific examples. We then proceed with our analytical approach in which we (i) derive a PDE which approximates the integral equation and (ii) show how an appropriate linearization of the PDE will lead to a prediction of the exact number of peaks that form when a circularly symmetric solution is unstable. At the end of section 3, we show how families of 3-bump, 7-bump, and 12-bump solutions form for a specific example. Section 4 gives a summary of our results and some directions for future study.

2. Background: One-dimensional models. Much of the present research into rate models stems from the early work of Wilson and Cowan [66] and subsequent studies by Amari [1, 2, 3] and Kishimoto and Amari [39]. These authors model the dynamics of a single layer of neurons
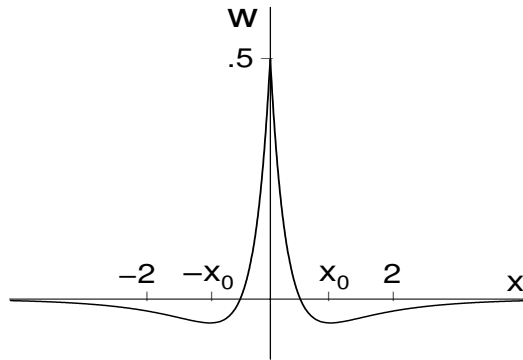
Figure 2.1. *An example of a coupling function giving "lateral inhibition" (positive for small $|x|$ and negative for large $|x|$).*

with rate equations of the form

$$(2.1) \qquad \frac{\partial u(x,t)}{\partial t} = -u(x,t) + \int_{-\infty}^{\infty} w(x-y) f(u(y,t))\, dy + s(x,t) + h.$$

Here $u(x,t)$ is the synaptic input to a neural element at time $t \geq 0$ and position $x \in (-\infty, \infty)$, $w(x)$ determines the coupling between elements, and $f(u)$ gives the firing rate of a neuron with input u. Neurons are said to be "active" if $f(u(x,t)) > 0$. The function $s(x,t)$ denotes a variable external stimulus, and h is a constant stimulus applied to the entire field.

In [2], Amari set $f(u) = H(u)$, where $H(u)$ is the Heaviside function, and assumed the following:

(H_1) $w > 0$ and $w' < 0$ on an interval $(0, \bar{x})$, $w(-\bar{x}) = w(\bar{x}) = 0$, and $w(x) < 0$ if $|x| > \bar{x}$.

(H_2) w is a continuous even function, and $\int_{-\infty}^{\infty} w(y)\, dy$ is finite.

An example of this "lateral inhibition"–type coupling is given in Figure 2.1. He then analyzes stationary solutions of (2.1) when $s(x,t) = 0$. Setting $\partial u(x,t)/\partial t = 0$ reduces (2.1) to

$$(2.2) \qquad u(x) = \int_{-\infty}^{\infty} w(x-y) H(u(y))\, dy + h.$$

The "region of excitation" of a stationary solution is the set $R(u) = \{x | u(x) > 0\}$. A 1-bump solution is a solution whose region of excitation is a finite interval. If the region of excitation consists of $N \geq 1$ disjoint finite intervals, then $u(x)$ is an N-bump solution. In [1, 2], Amari analyzes the existence, multiplicity, and stability of 1-bump solutions of (2.2).

In [43], we extended Amari's work and chose a specific $w(x)$, which changes sign infinitely often. For simplicity, we set $s(x,t) \equiv 0$ and studied

$$(2.3) \qquad \frac{\partial u(x,t)}{\partial t} = -u(x,t) + \int_{-\infty}^{\infty} w(x-y) f(u(y,t) - th)\, dy,$$

where

$$(2.4) \qquad w(x) = e^{-b|x|}(b \sin |x| + \cos x) \quad \text{and} \quad f(u) = 2e^{-\tau/u^2} H(u),$$

and b, th, and τ are positive constants. The parameter b controls the rate at which oscillations in w decay with x, th is the threshold (effectively replacing h in (2.1)), and τ controls the slope of $f(u)$. Note that $f(u)$ is a C^∞ extension of (twice) the Heaviside function when $\tau > 0$, and $f(u - th) = 0$ if $u \leq th$. An example of w and f are shown in Figure 2.2.
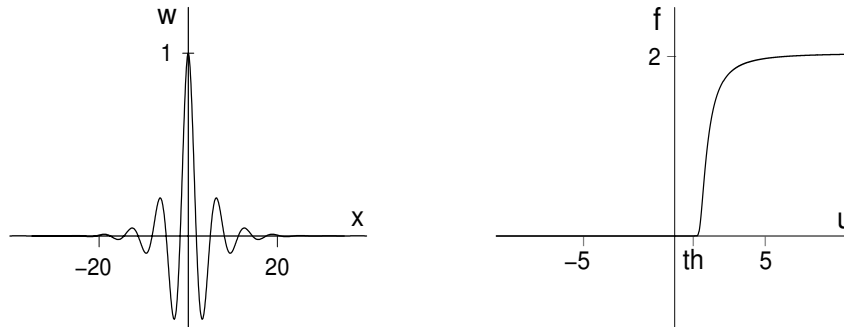

Figure 2.2. *Examples of $w(x)$ (left) and $f(u)$ (right) (2.4). Parameters are $b = 0.25$, $th = 1.5$, and $\tau = 0.005$.*

It is thought that the oscillatory form of coupling, (2.4), better represents the connectivity known to exist in the prefrontal cortex, where labeling studies have shown that coupled groups of neurons have "patchy" distributions, with a characteristic distance between patches [9, 34, 44].

As before, we define a stationary solution of (2.3)–(2.4) to be a solution of

$$(2.5) \qquad u(x) = \int_{-\infty}^{\infty} w(x - y) f(u(y) - th) \, dy.$$

To compare the two-dimensional results in the next section with the one-dimensional case, we give a brief derivation of the PDE and ODE which are equivalent to (2.3) and (2.5). We use the Fourier transform, defined by $\widehat{F}(g) = \int_{-\infty}^{\infty} e^{-i\alpha\eta} g(\eta) \, d\eta$, where $g \in L^1(\mathbb{R})$ and $\alpha \in \mathbb{R}$. Assume that u satisfies (2.5) and that u and u_t are continuous and integrable for $x \in \mathbb{R}$. Applying the Fourier transform to (2.3) and using its convolution property, we obtain

$$(2.6) \qquad \widehat{F}(u + u_t) = \widehat{F}(w)\widehat{F}(f(u - th)).$$

Evaluating $\widehat{F}(w)$ results in

$$(2.7) \qquad \widehat{F}(u + u_t) = \frac{4b(b^2 + 1)}{\alpha^4 + 2\alpha^2(b^2 - 1) + (b^2 + 1)^2}\widehat{F}(f(u - th)).$$

Next, multiplying (2.7) by $\alpha^4 + 2\alpha^2(b^2 - 1) + (b^2 + 1)^2$ and taking the inverse Fourier transform of both sides, we obtain the PDE

$$(2.8) \qquad (u + u_t)_{xxxx} - 2(b^2 - 1)(u + u_t)_{xx} + (b^2 + 1)^2(u + u_t) = 4b(b^2 + 1)f(u - th).$$

This PDE is exactly equivalent to the partial integro-differential equation (PIDE) (2.3). Using this equivalence and setting $u_t = 0$ in (2.8), we see that N-bump stationary solutions of (2.3)
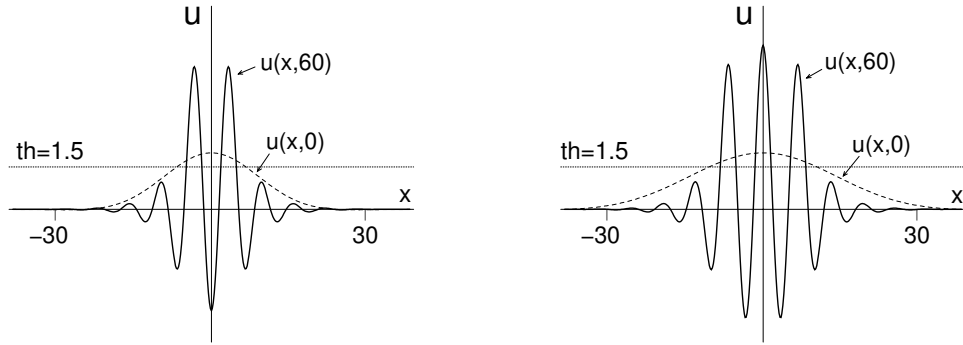
Figure 2.3. *Stable 2-bump (left) and 3-bump (right) solutions of* (2.3)–(2.4). *Parameters are* $\tau = 0.1$, $th = 1.5$, *and* $b = 0.25$.
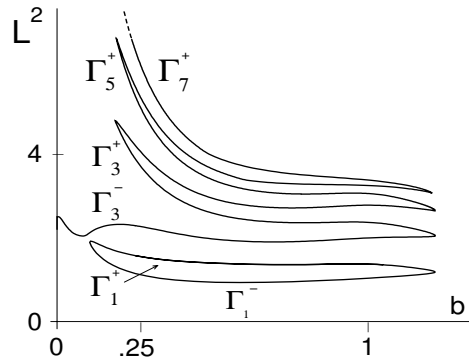
Figure 2.4. *Bifurcation diagram for N-bump solutions of* (2.9) *when N is odd. The vertical axis is the* L^2 *norm of the solution. Parameters are* $\tau = 0.1$, $th = 1.5$.

must satisfy the ODE problem

$$(2.9) \qquad \begin{cases} u'''' - 2(b^2 - 1)u'' + (b^2 + 1)^2 u = 4b(b^2 + 1)f(u - th), \\ \lim_{x \to \pm\infty}(u, u', u'', u''') = (0, 0, 0, 0). \end{cases}$$

In summary, by a judicious choice of coupling function w, we have exactly transformed the PIDE (2.3) into the PDE (2.8), whose stationary solutions satisfy the ODE problem (2.9). The new work in this paper consists of applying similar ideas to the two-dimensional system (1.1).

Numerical results. In [43], we solved (2.3) with initial conditions of the form

$$(2.10) \qquad u(x, 0) = \cos\left(\frac{Lx}{12.5\pi}\right)\exp\left(-\left(\frac{Lx}{12.5\pi}\right)^2\right), \quad -12.5\pi < x < 12.5\pi,$$

for different values of L (dashed curves in Figure 2.3). For appropriately chosen L, the initial condition evolves into a stationary N-bump solution which satisfies (2.9). To understand the global structure of solutions, we then used AUTO97 [22] to continue these N-bump solutions as b varied. This resulted in the bifurcation diagram shown in Figure 2.4, where Γ_N^+ and Γ_N^- are branches of stable and unstable N-bump solutions. (N is odd in this diagram—a similar

diagram showing families of N-bump solutions exists when N is even.) For $N \geq 3$, solutions arise at $b = 0$ through a bifurcation from a periodic orbit. Figure 2.4 suggests that a "snaking" phenomenon occurs in the branches of the bifurcation curve; solutions gain more bumps as the L^2 norm of the solution increases, with branches of stable solutions separated by branches of unstable solutions. See [43] for more details. Similar phenomena occur in other higher order ODE models [19, 38, 52]. For some applications, it is important to find ways to steer a system from one stable N-bump configuration to another. For example, switching from an N-bump to a 1-bump solution is of particular interest in the work of Thelen et al. [60], as it is proposed that this represents the process of decision-making by infants in the face of multiple choices.

3. The two-dimensional model. In this section, we analyze the formation of N-bump solutions in the two-dimensional model

$$(3.1) \qquad \frac{\partial u(x,y,t)}{\partial t} = -u(x,y,t) + \iint_\Omega w(x-q,y-s)f(u(q,s,t)-th)\,dq\,ds,$$

where $f(u)$ is a positive multiple of the firing function defined in (2.4) and $w(x,y)$ satisfies (1.5). Stationary solutions of (3.1) satisfy the associated equation

$$(3.2) \qquad u(x,y) = \iint_\Omega w(x-q,y-s)f(u(q,s)-th)\,dq\,ds.$$

For a given solution u of (3.2), we define its region of excitation to be

$$(3.3) \qquad R(u) = \{(x,y)|\ u(x,y) > th\}.$$

A solution of (3.2) is an N-bump solution if its region of excitation consists of N finite disjoint components.

We will address the following basic questions:
  (i) Is there a correspondence between families of N-bump solutions in one dimension and those in two dimensions? Do solutions exist in two dimensions that do not have one-dimensional counterparts?
  (ii) What are the dynamics responsible for the formation of N-bump solutions? How can we derive a PDE that is equivalent to (3.1)?

3.1. Numerical examples. Thus far we have numerical results for three specific systems [42, 43]. The first is (3.1) with $f(u) = H(u)$ and

$$(3.4) \qquad w(x,y) = Ke^{-k\sqrt{x^2+y^2}} - Me^{-m\sqrt{x^2+y^2}}.$$

In polar coordinates, (3.4) becomes $w(r) = Ke^{-kr} - Me^{-mr}$. If $K > M$ and $k > m$, then $w(r)$ has one positive zero. Figure 3.1 (upper left panel) shows a numerically stable 2-bump solution on a 10×10 square domain. Here $K = 3.5$, $k = 1.8$, $M = 2.8$, $m = 1.52$, and $th = 0$. In our study of the one-dimensional case, we found that stable 2-bump solutions could not exist for these parameter values, yet this computation suggests that stable 2-bump solutions do exist in two dimensions. We conjecture that this property can be explained using the analytical approach described in section 3.3.
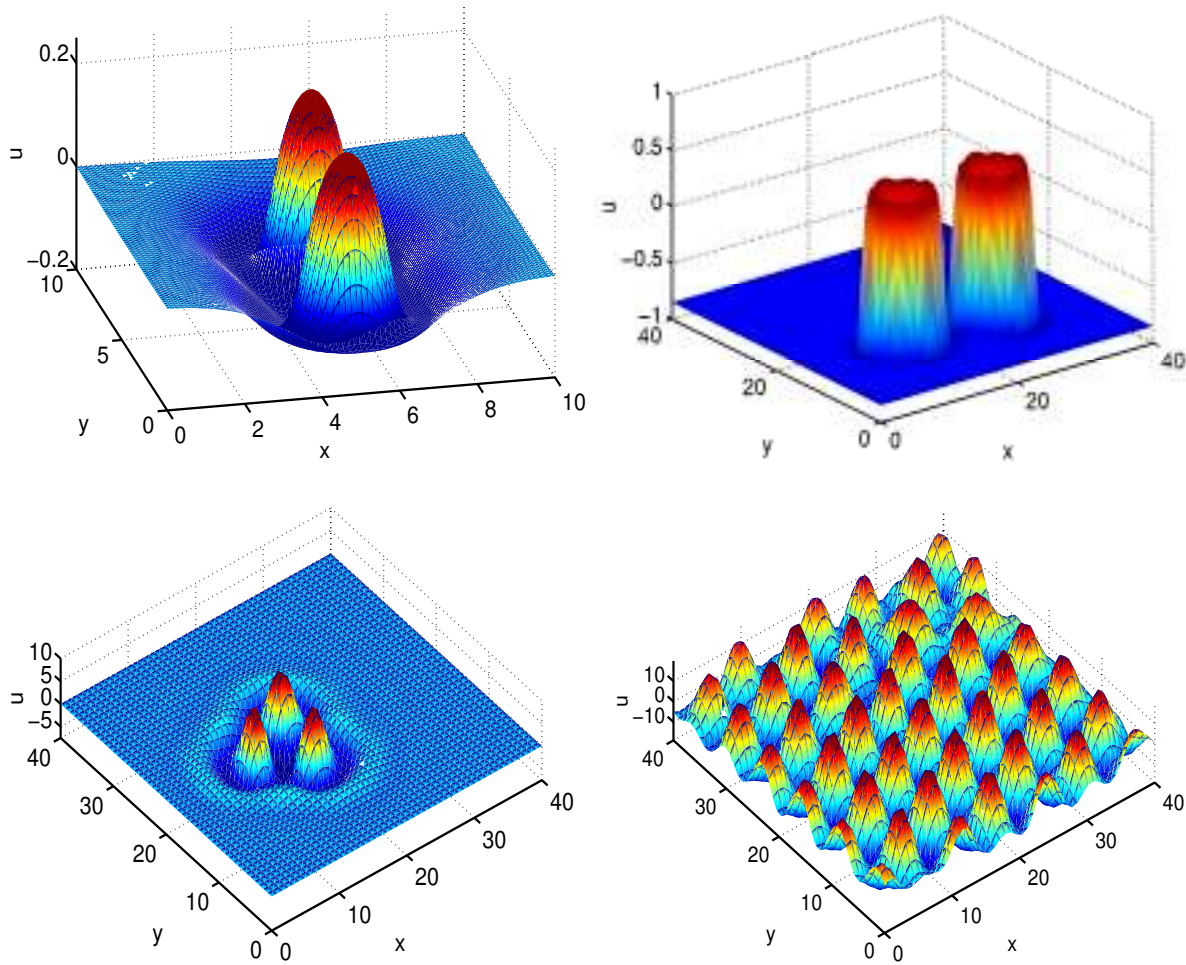
Figure 3.1. *Examples of multibump solutions for couplings* (3.4), (3.5), *and* (3.6). *See text.*

In our second example, we solve the two-dimensional analogue of (2.1) on a 40×40 grid with $f(u) = H(u)$, $s(x, t) \equiv 0$, and $h = -1$, and with the following coupling (studied in [42]):

$$(3.5) \qquad w(x, y) = 2e^{-k\sqrt{x^2+y^2}} \left[1 - d_1(x^2 + y^2) + d_2(x^2 + y^2)^2 - d_3(x^2 + y^2)^3 \right].$$

In polar coordinates, (3.5) becomes $w(r) = 2e^{-kr}(1 - d_1r^2 + d_2r^4 - d_3r^6)$. For the choice of parameters $(k, d_1, d_2, d_3) = (1, \frac{2}{3}, \frac{1}{18}, \frac{1}{1200})$ the function $w(r)$ has three positive zeros. Figure 3.1 (upper right) shows a numerically stable 2-bump solution for this case.

The third problem we have studied consists of (3.1), with the firing rate coupling (2.4) and with the coupling function

$$(3.6) \qquad w(x, y) = e^{-b\sqrt{x^2+y^2}} \left(b \sin\left(\sqrt{x^2 + y^2}\right) + \cos\left(\sqrt{x^2 + y^2}\right) \right),$$

where $b > 0$. The coupling in (3.6) is the two-dimensional analogue of (2.4). In polar coordinates, (3.6) becomes $w(r) = e^{-br}(b \sin r + \cos r)$, and $w(r)$ has infinitely many zeros. Figure 3.1 (lower panels) shows two numerically stable solutions computed on a square domain of size 40×40. For $b = 0.3$, the solution fills the entire domain with bumps (lower right panel). A similar "progressive recruitment" phenomenon is found by Gutkin, Ermentrout, and O'Sullivan in a one-dimensional model [34]. Usher, Stemmler, and Olami [62] found similar patterns in a stochastic model of spiking neurons that had short-range excitation and long-range inhibition. Raising b to $b = 0.4$, we find a 3-bump solution (lower left panel). As in the one-dimensional case, other N-bump solutions coexist.

3.2. Circularly symmetric solutions. Our numerical study shows that (3.1) has a rich structure of stable N-bump solutions for a wide range of coupling functions. In section 3.3, we will describe the fundamental role of circularly symmetric solutions in the formation of these solutions. To set the stage for section 3.3, our goal here is to summarize the important properties of the circularly symmetric solutions.

In polar coordinates, writing $x = r \cos \theta$, $y = r \sin \theta$, $q = \eta \cos \alpha$, $s = \eta \sin \alpha$, (3.1) becomes

$$(3.7) \quad \frac{\partial u(r, \theta, t)}{\partial t} = -u + \int_0^\infty \int_0^{2\pi} w\left(\sqrt{r^2 + \eta^2 - 2r\eta \cos(\theta - \alpha)}\right) f(u(\eta, \alpha, t) - th)\eta \, d\alpha \, d\eta.$$

Stationary solutions of (3.7) satisfy

$$(3.8) \quad u(r, \theta) = \int_0^\infty \int_0^{2\pi} w\left(\sqrt{r^2 + \eta^2 - 2r\eta \cos(\theta - \alpha)}\right) f(u(\eta, \alpha) - th)\eta \, d\alpha \, d\eta.$$

A solution is a circularly symmetric 1-bump solution if u is independent of θ and there is an $R_0 > 0$ such that

$$(3.9) \quad u(r) > th \text{ for } 0 < r < R_0, \quad u(R_0) = 0, \text{ and } u(r) < th \text{ for } r > R_0.$$

Since u is assumed to be independent of θ, we set $\theta = 0$, and (3.8) reduces to

$$(3.10) \quad u(r) = \int_0^{R_0} \int_0^{2\pi} w\left(\sqrt{r^2 + \eta^2 - 2r\eta \cos \alpha}\right) f(u(\eta, \alpha) - th)\eta \, d\alpha \, d\eta.$$

Thus a 1-bump circularly symmetric solution satisfies (3.9)–(3.10). When $N > 1$, circularly symmetric N-bump solutions are similarly defined.

Thus far, the only analytical results for circularly symmetric solutions are those given by Taylor [59] and Werner and Richter [65]. Taylor [59] discusses the case $f(u) = H(u)$, in which case $u(r)$ satisfies

$$(3.11) \quad u(r) = \int_0^{R_0} \int_0^{2\pi} w\left(\sqrt{r^2 + \eta^2 - 2r\eta \cos \alpha}\right) \eta \, d\alpha \, d\eta$$

for couplings of the form

$$(3.12) \quad w(r) = Ke^{-kr^2} - Me^{-mr^2},$$

where $K > M > 0$ and $k > m > 0$. He classifies some of the solutions and discusses their stability with respect to perturbations that vary only the radius of the solution. Werner and Richter [65] also discuss solutions of (3.11), in particular, circular and ring solutions, some of which were not found by Taylor. They also discuss the stability of these solutions with respect to perturbations that vary only the radius of the solution. In the next section, we will show how circularly symmetric N-bump solutions play an important role in the formation of asymmetric N-bump patterns.

We end this section by stating an open problem. Suppose that the region of excitation of a solution of (3.8) is a disc and that the firing rate function is a continuous increasing function of u. Then is it the case that u must be independent of θ? Or is it possible that there are coupling functions for which solutions exist which are not circularly symmetric? For elliptic PDEs the analogous problem of classifying positive solutions on a disc is very important and has been extensively studied [30, 57].

3.3. Noncircularly symmetric solutions: The PDE approach.
There have been few attempts to analyze solutions of (3.1) that do not have circular symmetry. Recently we have made progress on this problem by successfully deriving a PDE that is equivalent to the PIDE (3.1). We have also developed a method of analysis of the PDE which explains the formation of N-bump solutions similar to those in Figures 3.7, 3.8, and 3.12. Our approach is described below.

The first step is to apply the two-dimensional Fourier transform, defined by $F(g) \equiv (2\pi)^{-1} \int_{-\infty}^{\infty} \int_{-\infty}^{\infty} e^{-i(\alpha x + \beta y)} g(x, y) dx\, dy$ to (3.1). Note that $F(g)$ is a function of α and β. We obtain

$$(3.13) \qquad F(u + u_t) = F(w)F(f(u - th)).$$

For functions $w(x, y)$ that depend only on $\sqrt{x^2 + y^2}$, it is known that $F(w)$ is a function of $\sqrt{\alpha^2 + \beta^2}$ only. See Appendix A for a short proof. The coupling functions given in (3.4), (3.5), and (3.6) satisfy these properties. However, in each case $F(w)$ has a complicated form which prevents the use of (3.13) to derive a PDE. To circumvent this problem, we approximate $F(w)$ by a rational function, G, of $\sqrt{\alpha^2 + \beta^2}$ containing only even powers of its argument. The rationale behind this is the same as for the one-dimensional case: we are using the observation that $F(\nabla^2 f) = -(\alpha^2 + \beta^2)F(f)$.

We begin by choosing functions of the form

$$(3.14) \qquad G\left(\sqrt{\alpha^2 + \beta^2}\right) = \frac{A}{B + (\alpha^2 + \beta^2 - M)^2},$$

where A, B, and M are parameters. Once G is known, the approximate coupling function $\widehat{w}(x, y)$ is given by the inverse two-dimensional Fourier transform of it. Because of the symmetry of G, this reduces to a Hankel transform of order 0:

$$(3.15) \qquad \widehat{w}(r) = \int_0^{\infty} sG(s)J_0(rs)\, ds,$$

where J_0 is the Bessel function of the first kind of order zero (see Appendix A). In Figure 3.2, we illustrate an example of a coupling function $\widehat{w}$ when G is of the form (3.14). Note the similarity between this coupling function and the coupling function (3.6).
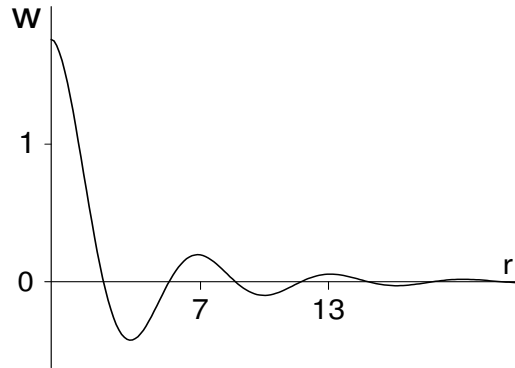
Figure 3.2. $\widehat{w}(r)$ (3.15) *for parameter values $M = 1$, $A = 0.4$, and $B = 0.1$.*

We now derive the PDE. First, replace $F(w)$ in (3.13) with (3.14). Next, multiply both sides of (3.13) by $B + (\alpha^2 + \beta^2 - M)^2$ and take the inverse two-dimensional Fourier transform to obtain

$$(3.16) \qquad \nabla^4(u + u_t) + 2M\nabla^2(u + u_t) + (B + M^2)(u + u_t) = Af(u(x, y, t) - th).$$

This equation is exactly equivalent to the PIDE (3.1) if w is given by (3.15), where $F(w)$ is given by (3.14). It is interesting to note that the derivative of u with respect to time cannot be separated from (3.16).

One can view this process of derivation of a PDE in two different ways. One is that, given a coupling $w(r)$, we can find its Fourier transform and then approximate that by an appropriate rational function of $\sqrt{\alpha^2 + \beta^2}$. This rational function can then be used to derive a PDE whose dynamics will in some way approximate the dynamics of the original PIDE. The other way to view it is that we *define $w(r)$* through (3.15) and, by varying the parameters A, B, and M in (3.14) (or in another appropriate rational function of $\sqrt{\alpha^2 + \beta^2}$), move through the space of possible coupling functions that can be treated this way. From this second point of view, there are no approximations made, but the tradeoff is that, by restricting G to be only rational functions of $\sqrt{\alpha^2 + \beta^2}$ with even powers of its argument, we may not be able to investigate all coupling functions $w(r)$ of interest. See section 3.5 for more discussion.

We now seek circularly symmetric solutions of (3.16). Under the assumption that u is not a function of θ, (3.16) becomes

$$\left[\frac{\partial^4}{\partial r^4} + \frac{2}{r}\frac{\partial^3}{\partial r^3} - \frac{1}{r^2}\frac{\partial^2}{\partial r^2} + \frac{1}{r^3}\frac{\partial}{\partial r} + 2M\left(\frac{\partial^2}{\partial r^2} + \frac{1}{r}\frac{\partial}{\partial r}\right)\right.$$

$$(3.17) \qquad \left. + B + M^2\right]\left(u + \frac{\partial u}{\partial t}\right) = Af(u - th).$$

Stationary solutions of (3.17) satisfy the ODE boundary value problem

$$(3.18) \qquad \begin{cases} u'''' + \frac{2}{r}u''' - \frac{1}{r^2}u'' + \frac{1}{r^3}u' + 2M\left(u'' + \frac{1}{r}u'\right) + (B + M^2)u = Af(u(r) - th), \\ u'(0) = u'''(0) = 0, \text{ and } \lim_{r \to \infty}(u, u', u'', u''') = (0, 0, 0, 0). \end{cases}$$

In order to determine the stability of a stationary solution $\widetilde{u}(r)$ of (3.17), we linearize the full PDE (3.16) around it. To do this, we follow [20] and write

$$(3.19) \qquad\qquad u(r,\theta,t) = \widetilde{u}(r) + \mu\nu(r,t)\cos(m\theta),$$

where μ is a small parameter, $\nu(r,t)$ is a perturbation function, and $m \geq 0$, an integer, is the azimuthal index. We choose this form of solution in order to investigate solutions that break the circular symmetry of the system. Substituting (3.19) into (3.16) and linearizing in μ, we obtain a PDE for ν:

$$
\begin{aligned}
&\left[\frac{\partial^4}{\partial r^4} + \frac{2}{r}\frac{\partial^3}{\partial r^3} + \left(\frac{2Mr^2 - 2m^2 - 1}{r^2} \right)\frac{\partial^2}{\partial r^2} + \left(\frac{2m^2 + 1 + 2Mr^2}{r^3} \right)\frac{\partial}{\partial r} \right. \\
(3.20) \qquad &\left. + \frac{m^4 - 4m^2 + (B + M^2)r^4 - 2Mm^2r^2}{r^4} \right]\left(\nu + \frac{\partial\nu}{\partial t} \right) = Af'(\widetilde{u} - th)\nu.
\end{aligned}
$$

Since this is a linear equation in ν, we expect the solution to be of the form $\nu(r,t) \sim \overline{\nu}(r)e^{\lambda t}$ as $t \to \infty$, where λ is the most positive (real) eigenvalue and $\overline{\nu}(r)$ is the corresponding eigenfunction. In order to determine the stability of a particular circularly symmetric solution with radial profile $\widetilde{u}(r)$, we substitute $\widetilde{u}(r)$ into (3.20), and for each integer $m \geq 0$ we find the largest value of $\lambda(m)$. Then we determine the positive integer N at which λ is the greatest. If $\lambda(N) > 0$, then the solution with radial profile $\widetilde{u}(r)$ is unstable. Our analysis predicts that N bumps will form if the initial condition for (3.16) consists of a small random perturbation of the circularly symmetric solution whose radial profile is $\widetilde{u}(r)$. The distance from the origin at which these N bumps appear is determined by the shape of the eigenfunction $\overline{\nu}(r)$ (see examples below).

To numerically determine λ and $\overline{\nu}(r)$, we integrated (3.20) with a randomly chosen initial condition $\nu(r,0)$. In general this is composed of many eigenfunctions, but due to the exponential growth or decay in time, for large t, $\nu(r,t)$ is dominated by the eigenmode with the most positive corresponding λ. The quantity λ can thus be determined by plotting the log of the norm of $\nu(r,t)$ as a function of time and measuring the slope of the corresponding graph after transients have died away. The eigenfunction $\overline{\nu}(r)$ is simply $\nu(r,t)$ when t is large, suitably scaled in amplitude if necessary. This process was repeated with a number of different random initial conditions to verify that they did not affect the determination of λ and $\overline{\nu}$. In all of our experiments, we found that the eigenfunctions either grew or decayed monotonically in time as $t \to \infty$. This reinforces our assumption that the dominant eigenvalue is real. It would be interesting to investigate this further and provide a proof to rigorously determine the nature of the dominant eigenvalue.

Below we use the procedures described above to compute specific multibump solutions. To solve the PDEs (3.17) and (3.20), we used a finite difference scheme with 100 equally spaced r values in the interval $(0, 30]$ and an Euler step in time of length $dt = 0.5$. Boundary conditions were $u = \partial u/\partial r = 0$ at $r = 30$. We solved the full PDE (3.16) on the disc $\Omega = \{(r,\theta)|0 \leq r \leq 30,\ 0 \leq \theta \leq 2\pi\}$ with boundary conditions $u = \partial u/\partial r = 0$ at $r = 30$ for all $\theta \in [0, 2\pi]$. Here we also used a finite difference scheme, discretizing the disc Ω into a 100×90 grid of (r,θ) values. In the t direction we again used an Euler step of length $dt = 0.5$. The results shown were insensitive to changes in the time-step size, the number of points used

in the spatial discretization, and whether finite-difference or spectral methods [61] were used to approximate the spatial derivatives.

3.4. Examples of multibump formation. In this section, we demonstrate how three different families of multibump solutions form. The first is a 3-bump solution, the second is a 12-bump solution, and the third is a 7-bump solution. Throughout we use the parameter values $M = 1$, $A = 0.4$, and $B = 0.1$ in (3.14). For the firing rate we use

$$(3.21) \qquad f(u) = e^{-\tau/u^2} H(u).$$

This function is a scalar multiple of the function in (2.4) and is a natural extension of the Heaviside function $H(u)$ (i.e., (3.21) reduces to the Heaviside function when $\tau = 0$). We fix $\tau = 0.1$ in (3.21). The first step is to find a circularly symmetric solution. For this we set $th = 0.25$ and solve (3.17) to obtain the solution shown in Figure 3.3 (left, solid curve). Note that this is only one of a number of stable solutions; it was selected by letting the initial condition $u(r, 0)$ be an appropriately chosen Gaussian.
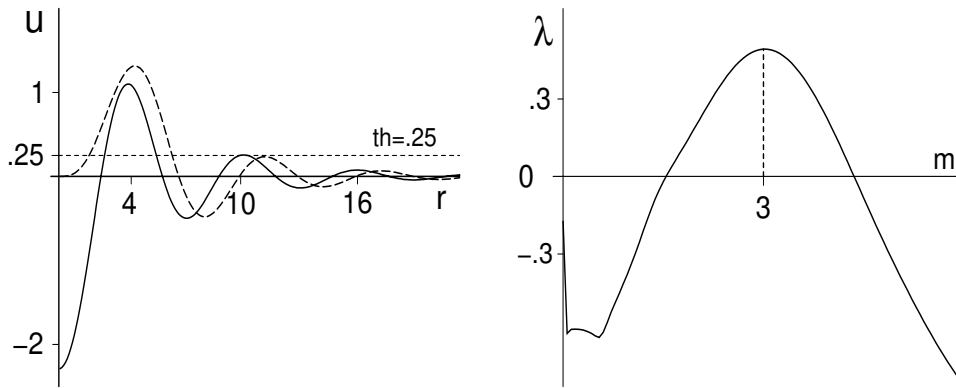

Figure 3.3. *Left: Stable solution of* (3.17) *(solid curve, defined as γ_1 in the text), and the eigenfunction corresponding to $m = 3$ (dashed). The solution is the one at P_1 in Figure* 3.4. *Right: λ as a function of m for the solution in the left panel.*

Next, we use AUTO97 [22] (applied to the system (3.18)) to continue this solution as the parameter th varies. Figure 3.4 shows the resulting bifurcation curve. The vertical axis is the maximum value of a solution, and the horizontal axis denotes the parameter th. The bifurcation curve has multiple folds (compare with Figure 2.4), and solutions gain more bumps as $u_{\max}$ increases. For example, at $th = 0.25$ there are several coexisting solutions, three of which are denoted by the points P_1, P_2, and P_3.

The solutions corresponding to these points are shown in Figures 3.3, 3.5, and 3.6, respectively. We have studied the stability of these solutions using (3.20), and for each we have computed the corresponding function $\lambda(m)$, shown in the right panels of Figures 3.3, 3.5, and 3.6.
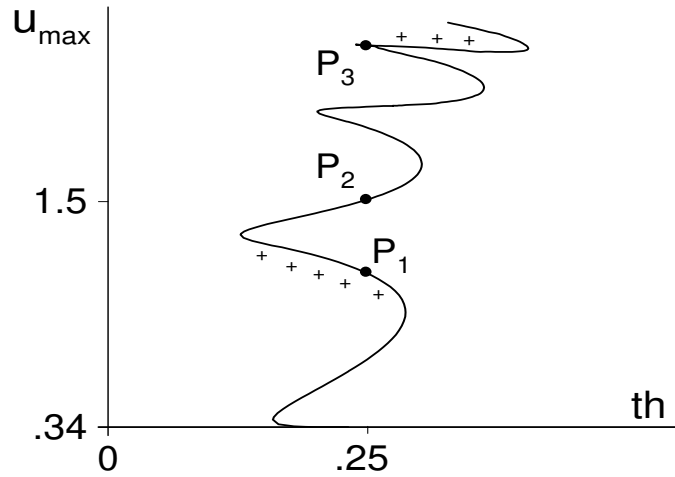
Figure 3.4. *Bifurcation diagram for solutions of* (3.18) *satisfying* $u(0) < 0$ *and* $u''(0) > 0$. *The solutions at* P_1, P_2, *and* P_3 *are shown in Figures* 3.3, 3.5, *and* 3.6, *respectively. Branches marked with a "+" sign are stable solutions of* (3.17).
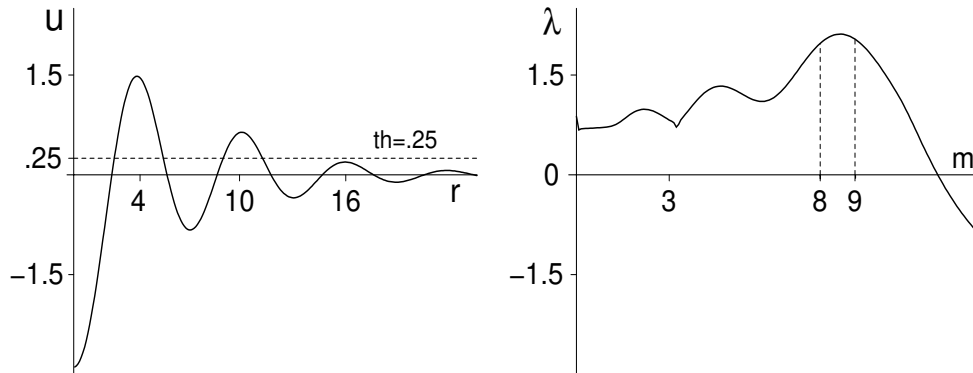
Figure 3.5. *Left: Unstable stationary solution of* (3.17) *corresponding to the point* P_2 *in Figure* 3.4. *The dashed line is* $u = th$. *Right:* λ *vs.* m *for the solution in the left panel. Note that* $\lambda(0) > 0$, *and hence we see the instability of the solution.*

3.4.1. The formation of a 3-bump solution. Define γ_1 to be the solution of (3.18) shown with a solid curve in the left panel of Figure 3.3 and Γ_1 to be the surface obtained by rotating γ_1 through a full circle about the line $r = 0$. Note that the positive parts of Γ_1 form a set of concentric annuli (see Figure 3.7, top left). Figure 3.3 (right panel) shows that for γ_1, $\lambda < 0$ when $m = 0$. This implies that γ_1 is actually a stable solution of (3.17). (Indeed it must be, as we found it by numerically integrating (3.17).) We also see that $m = 3$ is the integer with the largest value of λ and that $\lambda(3)$ is positive. The eigenfunction corresponding to $m = 3$ is shown in the left panel of Figure 3.3 (dashed curve). Its largest peak is centered over the
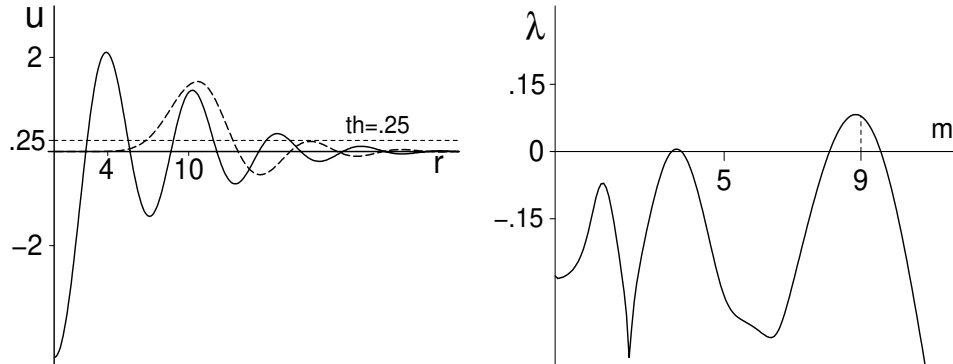
Figure 3.6. *Left: Stable stationary solution of* (3.17) *(solid curve) corresponding to* P_3 *in Figure* 3.4 *(defined to be* γ_3 *in the text), and the eigenfunction corresponding to* $m = 9$ *(dashed). Right:* λ *vs. m for the solution in the left panel.*

first positive bump of γ_1. Therefore, we expect any instability of Γ_1 in the full PDE (3.16) to have three-fold rotational symmetry and to appear at the annular part of Γ_1 corresponding to the first positive bump of γ_1. That is, if the initial condition of (3.16) is a small perturbation from Γ_1, we predict that the resulting solution will evolve into a 3-bump solution. Figure 3.7 illustrates that this is what happens. The upper left panel shows the initial condition, a small random perturbation of Γ_1 (the circularly symmetric solution generated by rotating γ_1 through a full circle). The next two panels illustrate the formation of a 3-bump solution as t increases from $t = 0$ to $t = 30$. If the integration is continued past $t = 30$, the 3-bump solution stimulates nearby regions and more bumps form, eventually filling the entire region (not shown). The resulting pattern is similar to that seen in the lower right panel of Figure 3.1. However, if we raise the threshold from $th = 0.25$ to $th = 0.3$ at $t = 30$, the nearby regions are *not* sufficiently stimulated, and the (now stable) 3-bump pattern persists (compare with Figure 3.1, lower left).

We now briefly describe properties of the solution corresponding to P_2, shown in the left panel of Figure 3.5. This solution has two intervals on which $u > th$ and is an *unstable* solution of (3.17) since $\lambda(0) > 0$. Note that we had to use AUTO97 to find this solution due to its instability. (Note also that it is not a stable solution of (3.16)).

3.4.2. The formation of a 12-bump solution. We now focus on the stationary solution of (3.17), which we define as γ_3, corresponding to the point P_3 in Figure 3.4 (see Figure 3.6). Upon rotation through a full circle about the line $r = 0$, γ_3 generates the multiring annular solution which we define to be Γ_3, similar to that shown in the upper left panel of Figure 3.8. γ_3 is a stable solution of (3.17) since $\lambda(0) < 0$. However, it is an unstable solution of (3.16) since for some m, $\lambda(m) > 0$. (Indeed, $m = 9$ is the integer with the largest positive λ.) The eigenfunction corresponding to $m = 9$ is shown dashed in Figure 3.6 (left). The largest peak of the eigenfunction is centered over the second positive bump of γ_3. Thus, if a small perturbation of Γ_3 was used as the initial condition for (3.16), we predict that the solution
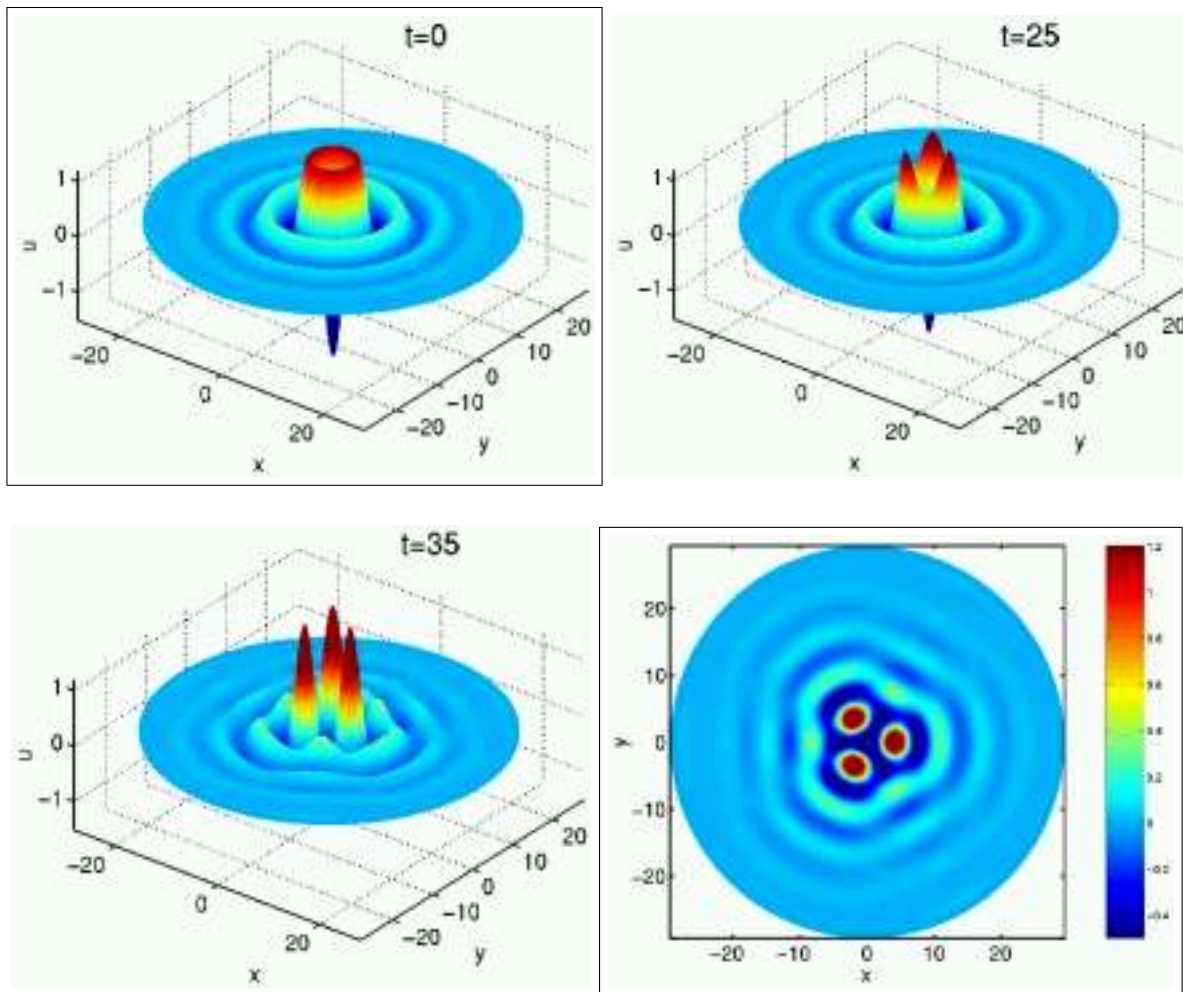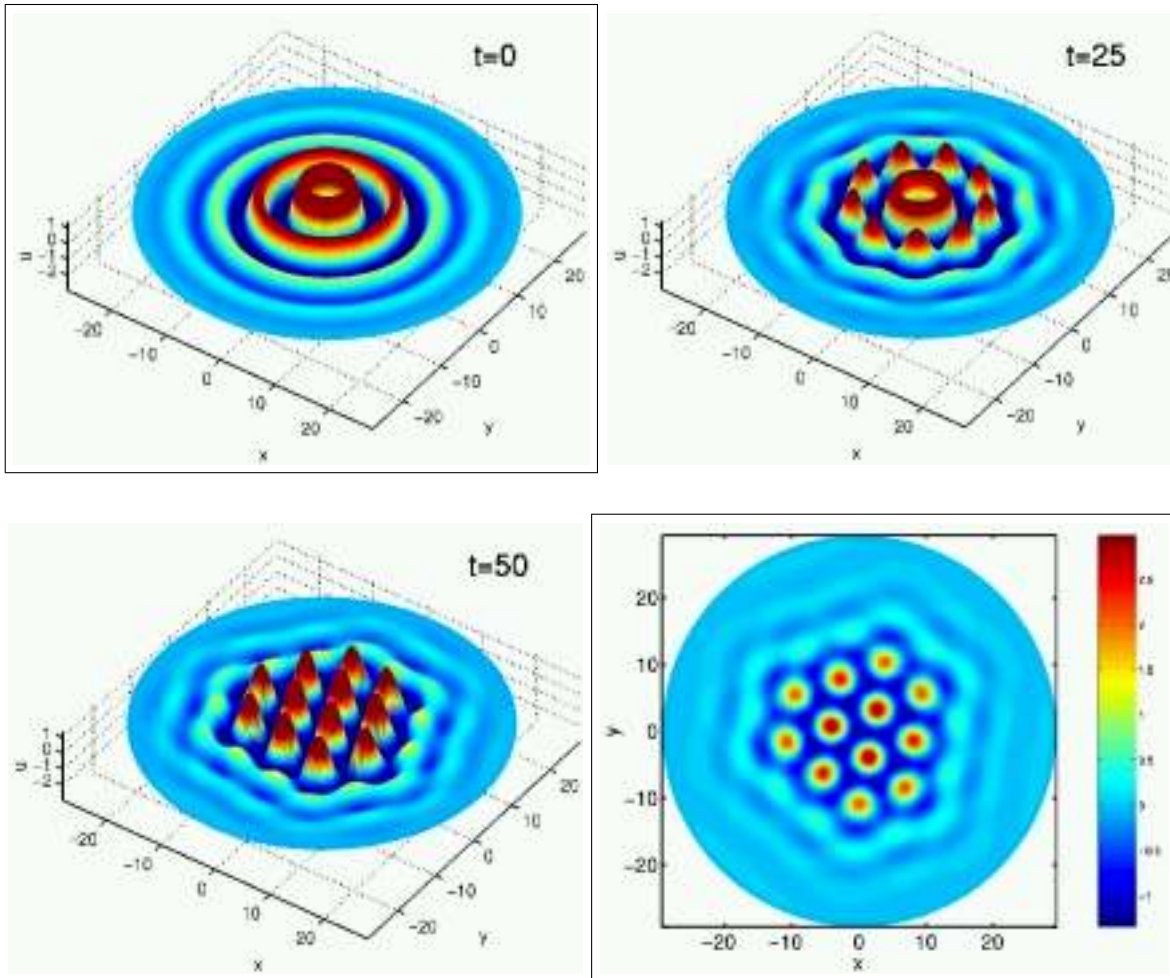
Figure 3.7. *The 3-peak solution resulting from the instability of the circularly symmetric solution whose radial profile is given by the solid curve in Figure 3.3 (left). Top left: Initial condition (a small random perturbation of Γ_1). Top right: At $t = 25$. Bottom left: At $t = 35$. Bottom right: Level curve diagram at $t = 35$. Clicking on the top left or bottom right panels will show movies of the development of the solution from different viewpoints.*

would develop 9-fold rotational symmetry, with the nine new bumps appearing in place of the annulus corresponding to the second positive bump of γ_3. That is, we predict that the second ring will break into nine bumps. In Figure 3.8 we see that this is what happens. As t increases from $t = 0$ to $t = 25$, the inner ring retains its circularly symmetric structure.

Although it is not easily seen in Figure 3.8, there is a subtle two-step process that happens next. First, as t increases from $t = 25$, the amplitude of the inner ring shrinks until the inner ring (taken in isolation) is the same size as the single ring shown in the upper left panel of Figure 3.7. (Recall that this solution corresponds to the point P_1 in Figure 3.4.) After this point, the inner ring begins its evolution into a 3-bump structure, while the outer nine bumps remain (lower panels of Figure 3.8). To understand the "shrinking" phenomenon, we have a

Figure 3.8. *The formation of a 12-peak pattern resulting from the instability of the circularly symmetric solution whose radial profile is given by the solid curve in Figure 3.6 (left), the axially symmetric solution at* P$_3$*. Top left: Initial condition (a small random perturbation of* Γ$_3$*). Top right: $t = 25$. Lower panels: $t = 50$ (left), and corresponding level curve diagram (right). Clicking on the top left or bottom right panels will show movies of the development of the solution from different viewpoints.*

plausible explanation based on the following calculation: First, we let the initial condition for a solution of (3.17) consist of the function which is equal to γ_3 until its first negative-going zero crossing and which is zero otherwise. (This initial condition is shown dashed in Figure 3.9.) Next, we solved (3.17) with this initial condition and found that the solution quickly shrank in amplitude and evolved into γ_1 (shown in Figure 3.3), which corresponds to the point P$_1$ in Figure 3.4. Since we know that Γ$_1$ breaks into a 3-peak structure under the dynamics of (3.16), we expect the "shrunken" inner ring to begin breaking into a 3-peak structure as t increases further. Figure 3.8 shows that this is indeed what happens.

3.4.3. The formation of a 7-bump solution. For our third example, we consider the class of circularly symmetric solutions consisting of a central peak surrounded by one or more
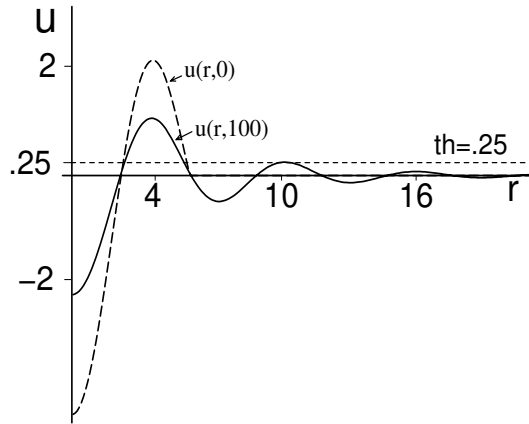
Figure 3.9. *The dashed curve shows the initial condition for* (3.17) *(its construction is given in the text), and the solid line shows the stable stationary state,* $u(r, 100)$. *The line* $u = th$ *is also shown.*
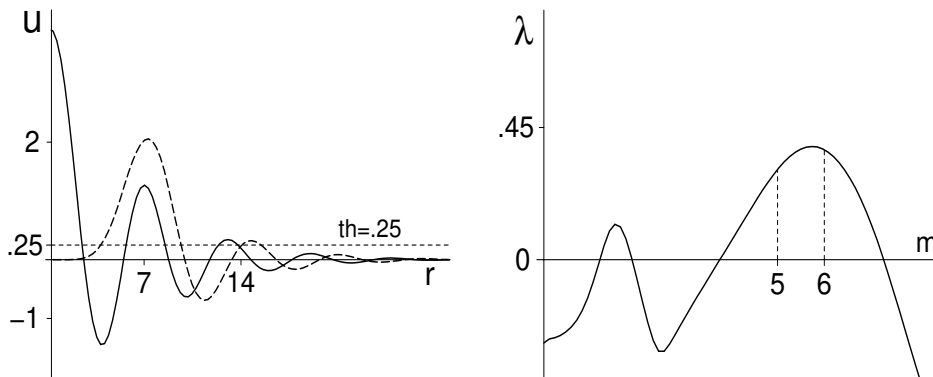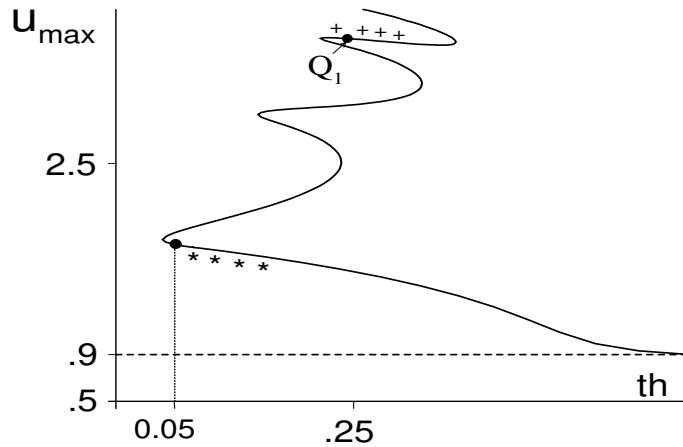

Figure 3.10. *Left: Stable solution of* (3.17) *(solid, defined as* γ_4 *in the text) corresponding to the point* Q_1 *in Figure* 3.11, *and the eigenfunction (dashed) corresponding to* $m = 6$. *Right:* λ *as a function of* m *for the solution in the left panel. Parameters are* $th = 0.25$, $M = 1$, $A = 0.4$, $B = 0.1$, $r = 0.1$.

annular rings. To find one such solution we again set $th = 0.25$ and solved (3.17). The resulting curve is shown (solid line) in Figure 3.10 (left). We denote it by γ_4 and denote by Γ_4 the surface produced by rotating γ_4 through a full circle about the line $r = 0$ (Figure 3.12, upper left). The initial condition was chosen so that the system (3.17) approached a solution with $u(0) > 0$, in contrast with the solutions previously studied in this section.

The solution γ_4 satisfies the ODE (3.18) with initial conditions of the form

(3.22) $$u(0) > 0, \ u'(0) = 0, \ u''(0) < 0, \ u'''(0) = 0.$$

As in the previous examples, we use AUTO97 to continue the solutions of (3.18) as the

Figure 3.11. *Bifurcation diagram for solutions of* (3.18) *satisfying* $u(0) > 0$ *and* $u''(0) < 0$. *The solution at* Q_1 *is shown in Figure* 3.10 *(left). The "+" signs indicate that a particular branch is a stable solution of* (3.17). *The "∗" signs indicate stable solutions of* (3.16), *i.e.,* $\lambda < 0$ *for all* m. *At the critical value* $th \approx 0.05$, *there is a change in stability. See text.*

parameter th varies. Figure 3.11 gives the resultant bifurcation curve. Again, the curve has multiple folds, and solutions gain more bumps as u_{max} increases (compare with Figure 3.4). The point Q_1 in Figure 3.11 represents γ_4. We numerically solve (3.20) with $\widetilde{u} = \gamma_4$ to determine its stability. The corresponding plot of λ as a function of m is shown in Figure 3.10 (right). We see that γ_4 is a stable solution of (3.17) since $\lambda < 0$ when $m = 0$. However, Γ_4 is an unstable solution of (3.16) since $\lambda > 0$ for some $m > 0$. ($m = 6$ is the integer with the largest positive λ.) The eigenfunction corresponding to $m = 6$ is shown dashed in Figure 3.10 (left). Its largest component is concentrated near the second positive bump of γ_4, corresponding to the innermost annular ring of Γ_4. Thus, if the initial condition of (3.16) is a small random perturbation of Γ_4, we expect the innermost annular ring of the solution to break into six bumps, which will surround the central peak, resulting in a total of seven bumps. Figure 3.12 shows that this is indeed what happens.

3.4.4. Discussion. In this section, we have investigated the formation of three particular multibump patterns. These are not the only three, as there are many more solutions of (3.18), with more superthreshold oscillations before their decay to zero at $r = \infty$. These can presumably be analyzed in the same way as we have done here and will all lead to different patterns being formed.

We have presented one particular way of forming multibumps here, namely, finding circularly symmetric solutions that are unstable with respect to perturbations that break the circular symmetry and using small perturbations of these circularly symmetric solution as initial conditions for fixed parameter values. Another, perhaps more realistic, way of causing these patterns to form is to find circularly symmetric solutions of (3.16) that are stable with respect to perturbations that break the circular symmetry (i.e., have $\lambda < 0$ for all m) and
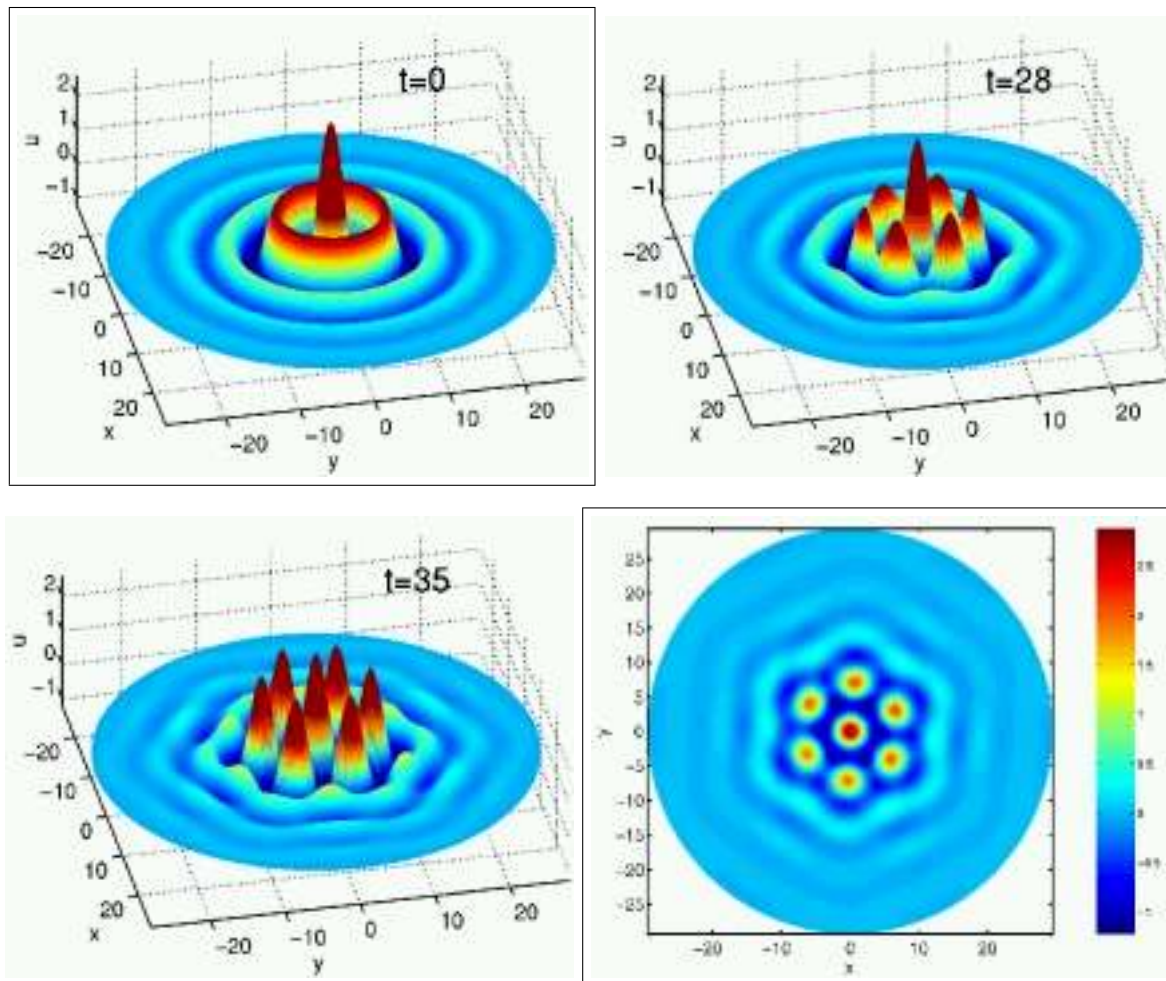
Figure 3.12. *The 7-peak solution resulting from the instability of the circularly symmetric solution whose radial profile is given by the solid curve in Figure 3.10 (left), the axially symmetric solution at Q_1. Top left: Initial condition (a small random perturbation of Γ_4). Top right: $t = 28$. Lower panels: $t = 35$ (left), and corresponding level curve diagram (right). Clicking on the top left or bottom right panels will show movies of the development of the solution from different viewpoints.*

then vary the parameters in such a way as to make the solution unstable with respect to these perturbations. This can be thought of as mimicking the change in the bulk properties of the neural tissue that would result from, for example, the action of neuromodulators (see, for example, [32].)

As an example, in Figure 3.13 we show a solution of (3.17) with $th = 0.08$ corresponding to the lowest branch in Figure 3.11. The corresponding plot of λ as a function of m is shown in Figure 3.14 (squares). We see that $\lambda < 0$ for all m, and thus the circularly symmetric solution formed by rotating the curve in Figure 3.13 through a full circle about the line $r = 0$ is a stable solution of (3.16). We now decrease th. The solution shown in Figure 3.13 changes very little, but its stability changes markedly. In Figure 3.14, we show plots of λ as a function
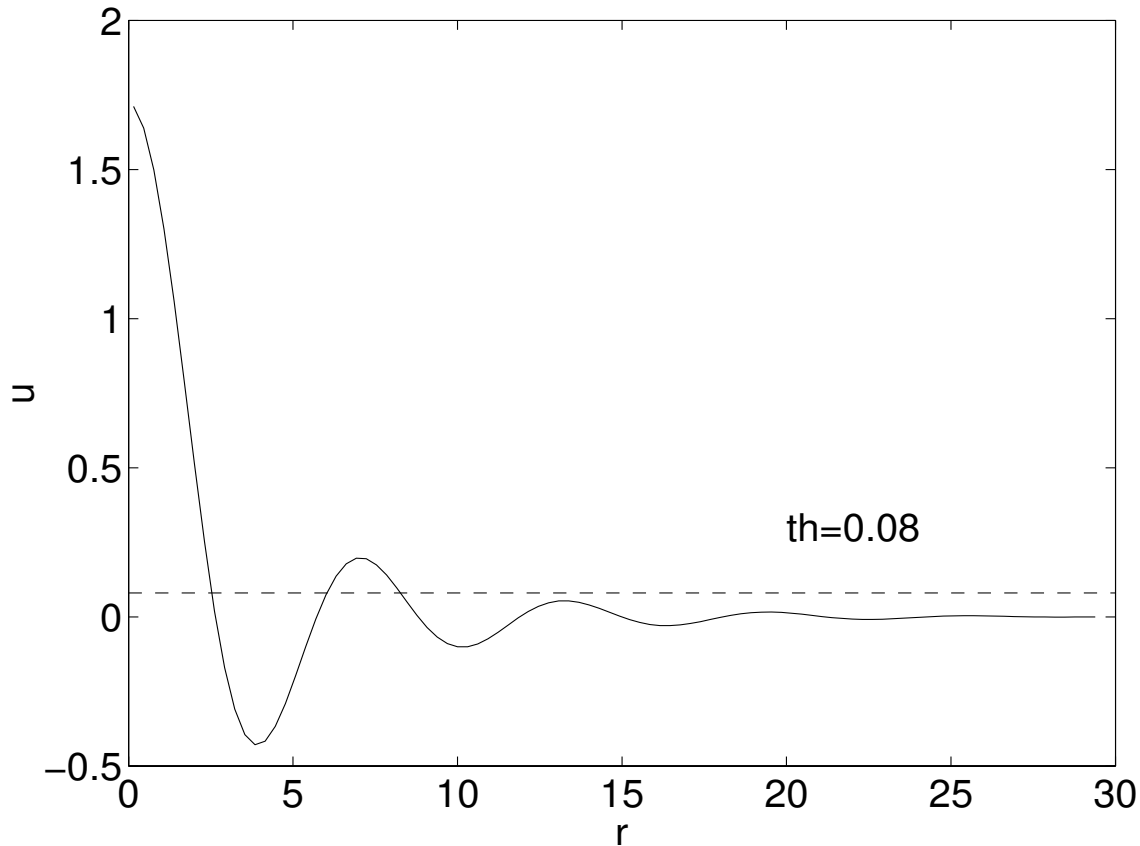
Figure 3.13. *A stable solution of* (3.17). *Parameter values are* $A = 0.4$, $B = 0.1$, $M = 1$, $r = 0.1$, $th = 0.08$.

of m for $th = 0.0536$ and $th = 0.046$. As th is decreased, the solution becomes unstable at $th \approx 0.05$ (see Figure 3.11), with $m = 6$ being the integer with the most positive value of λ. The eigenfunction corresponding to $m = 6$ has its largest peak near the bump of the solution in Figure 3.13 between $r = 5$ and $r = 10$ (not shown).

Thus we expect that if the initial condition of (3.16) is a small perturbation of the circularly symmetric surface with radial profile given by the solution in Figure 3.13 and at some point in the simulation th is reduced sufficiently from $th = 0.08$, we should see a breakup of the solution in a way similar to that shown in Figure 3.7. This is indeed what is seen (not shown).

3.5. General couplings. In this paper we have investigated one particular family of coupling functions, defined through their Fourier transform (3.14). However, a number of other types of coupling functions have been studied in the past, notably "Mexican hat"–type coupling [26, 31, 50]. (Examples are a difference of Gaussians [40, 55] and a difference of exponentials [6, 16, 33, 42].) Gaussian functions have also been used [35, 53, 54, 64] as have sinusoidal functions on a periodic domain [37, 41] and general nonnegative even functions [5, 7, 8, 27]. Specific nonneural applications whose models involve these types of coupling function include martinsitic phase transitions in steel, the behavior of diblock copolymers, and population
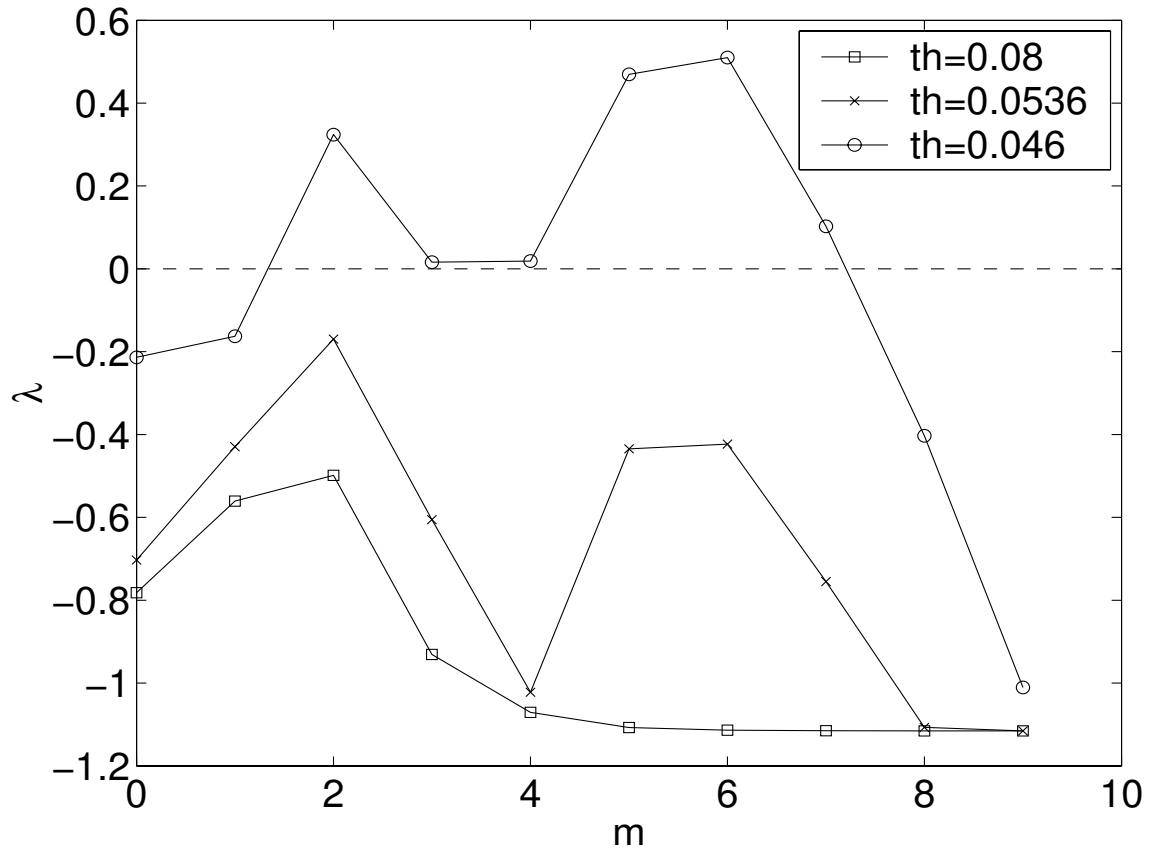
Figure 3.14. λ *as a function of m for three different values of th.*

dynamics. We now show that our technique of approximating the Fourier transform of the coupling function so that a PDE can be derived can also be applied to these types of coupling.

First consider a two-dimensional coupling function whose radial dependence is Gaussian. Since the two-dimensional Fourier transform of such a function is also circularly symmetric with a Gaussian dependence on distance in Fourier space, the problem reduces to approximating a one-dimensional Gaussian in η by a rational function of η^2. For concreteness, choose $F(\eta) = \exp(-\eta^2)$. Figure 3.15 shows the Gaussian for $0 < \eta < 4$ and two approximations to it. One approximation is a Padé approximant, a generalization of a Taylor series that matches F and as many derivatives at $\eta = 0$ as possible. This approximant is of degree $(0, 4)$, as the numerator is a polynomial of degree 0 and the denominator is of degree 4. (Note that due to the evenness of the Gaussian, only even powers of η will appear in the approximant, automatically satisfying the general condition that only even powers appear in the approximation of the Fourier transform of the coupling function.) The other function shown is the least squares fit of a function of the form $a_1/(a_2 + a_3\eta^2 + a_4\eta^4)$ to 100 evenly spaced points on the Gaussian curve. Note that these coefficients will change if the domain over which the Gaussian is considered is changed. Both of the approximations presented here are good and can be used to derive a fourth order PDE. Since both approximations have numerators of or-
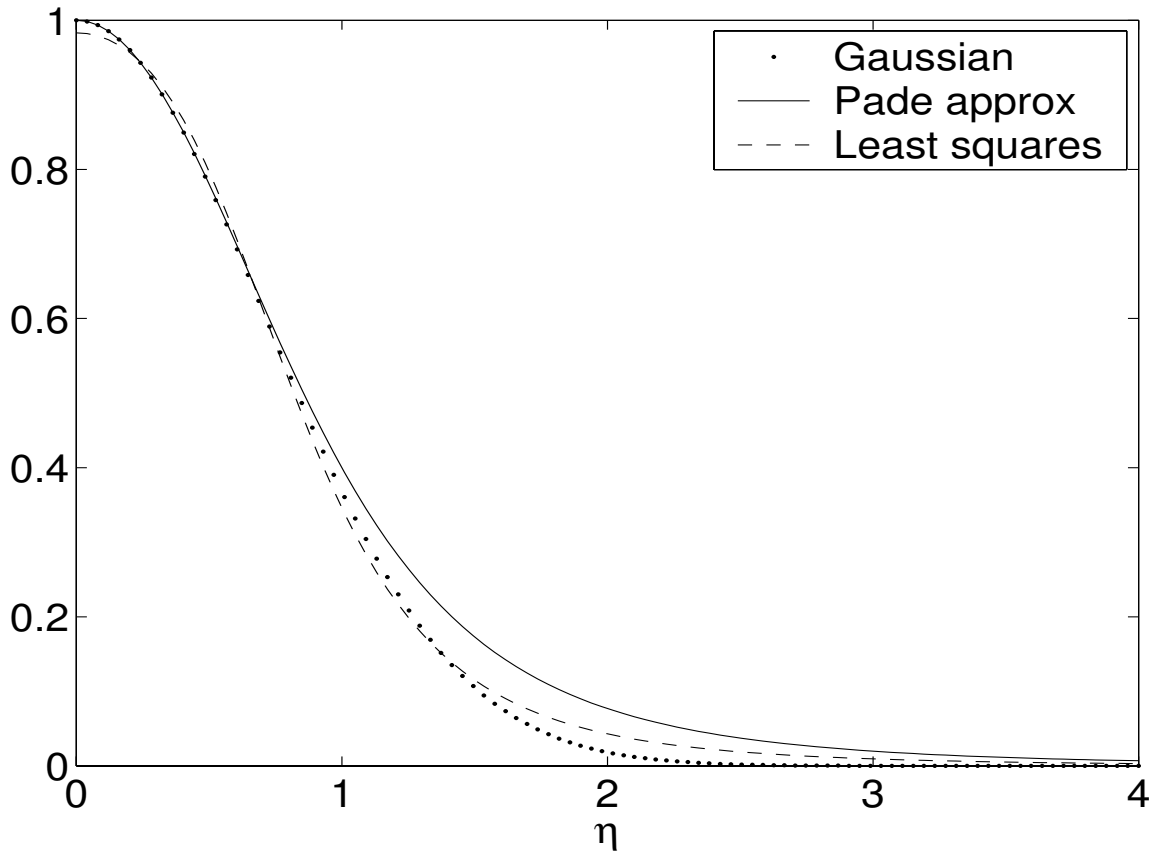
Figure 3.15. *Dotted: The Gaussian* $\exp\left(-\eta^2\right)$. *Solid: The Padé approximant* $1/(1 + \eta^2 + \eta^4/2)$. *Dashed: The least squares approximation* $2.7287/(2.7758 + 1.7504\eta^2 + 3.3574\eta^4)$.

der zero, the right-hand side of the corresponding equation of the form (3.16) will not contain spatial derivatives. Clearly, as either the degree of the Padé approximant or the degree of the rational function that is fit to the Fourier transform of the coupling function is increased, the approximation will become better and the order of the resulting PDE will rise.

Since taking the Fourier transform is a linear operation, coupling functions formed from the difference of Gaussians can be dealt with using the ideas just presented.

As a second example, we consider a difference of exponentials of the same form as (3.4). We need to find the two-dimensional Fourier transform of the function

$$(3.23) \qquad w(r) = Ke^{-kr} - Me^{-mr},$$

where $M < K$, $m < k$, and r is the radius. From the result in Appendix A, we have

$$(3.24) \qquad F(w)(\eta) = \int_0^\infty \left[Ke^{-kr} - Me^{-mr}\right] J_0(r\eta)r\,dr,$$

where J_0 is the Bessel function of first kind of order 0. Using the results of Appendix B, we
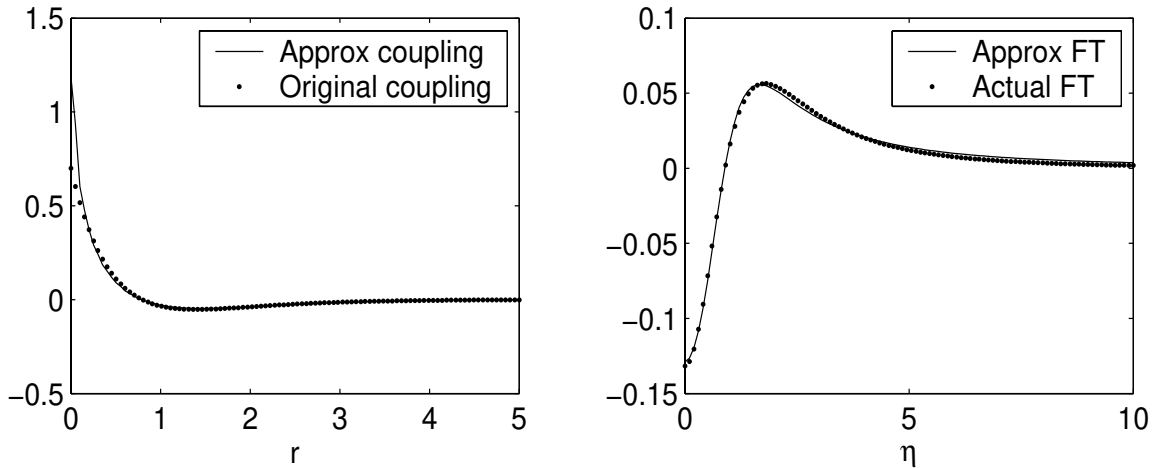
Figure 3.16. *Left: The coupling function* (3.23) *(dotted), and the inverse Fourier transform of the function shown solid in the right panel (solid). Right: The exact Fourier transform of w, given by* (3.25) *(dotted), and its approximation* (3.26) *(solid).*

have

$$(3.25) \qquad F(w)(\eta) = \frac{Kk}{(k^2 + \eta^2)^{3/2}} - \frac{Mm}{(m^2 + \eta^2)^{3/2}}.$$

We set $K = 3.5$, $M = 2.8$, $k = 1.8$, and $m = 1.52$, the values used in section 3.1. In Figure 3.16 (left, dotted) we show the coupling function $w(r)$, and in the right panel (dotted) we show its exact Fourier transform (3.25). We have approximated (3.25) by an appropriate rational function of η, minimizing the least squares error for the data shown in Figure 3.16, right. The result is

$$(3.26) \qquad G(\eta) = \frac{1.2636\eta^2 - 1}{7.7592 + 4.1991\eta^2 + 3.3163\eta^4}.$$

This function is shown with a solid curve in Figure 3.16, right. In the left panel of Figure 3.16, we show the coupling function resulting from taking the inverse Fourier transform of $G(\eta)$, given by (3.15) (solid line). We chose a rational function of the form (3.26) as it gave a good approximation. Using higher order polynomials (with even powers of η) in the numerator and denominator of the approximation would result in a better approximation of w by $\widehat{w}$ but would also result in higher order PDEs. Clearly, the coupling in (3.26) can be used to derive a fourth order PDE for u, and the dynamics of this equation will be equivalent to the integral equation (3.1) for the coupling shown with the solid curve in Figure 3.16 (left).

4. Summary. In this paper we have studied a class of PIDEs which have been used extensively in neuronal modeling. Our goal throughout has been to develop methods which help us understand the dynamics of multibump formation in two space dimensions.

Section 2 summarizes results for the model in one space dimension. These include the existence, multiplicity, and stability of N-bump solutions. In section 3, we focus on the two-dimensional model. This part of our investigation has led to the following results:

(i) the development of a method to approximate a PIDE with a PDE;

(ii) a description of the important properties of circularly symmetric solutions of the PDE;

(iii) the development of a method to analyze the PDE and determine the stability of circularly symmetric solutions. For unstable solutions, our methods predict the exact number of bumps that form as the unstable solution evolves.

We then applied these techniques to a specific equation and illustrated the dynamic formation of multibump solutions in three different scenarios. Finally, in section 3.5, we discuss the feasibility, both numerical and theoretical, of extending our methods to models with other couplings.

Similar results regarding the breakup of annular rings include [20], in which the stability of higher-bound states in self-focusing optical media is studied, and [46], in which the breakup of concentric rings in a reaction-diffusion system is studied. Both of these examples involve PDEs, and our results appear to be the first for integro-differential equations.

A first step in making our methods mathematically rigorous is to prove the existence of the fundamentally important solutions of the ODE problem (3.18). These describe circularly symmetric solutions of the PDE. This problem is especially challenging since (3.18) is nonautonomous and is neither reversible nor Hamiltonian. One approach is to cast (3.18) as a two-dimensional shooting problem. Here the two free parameters are the values of $u(0)$ and $u''(0)$. Note that while the relationship between homoclinic orbits and spatially localized patterns in one dimension is well known [14, 38, 43], we use such orbits here to find patterns in two spatial dimensions.

Another issue to be addressed is the correspondence between solutions of the PDE (3.16) and the integral equation (3.1), when the coupling function is given by (3.15). Formally, the equations are equivalent, but it remains to be proven that solutions of one are also solutions of the other, and if so, whether stability of a solution of one equation implies stability of that solution from the point of view of the other equation. We have not attempted to numerically solve the integral equation (3.1).

There are several ways to extend the techniques developed in this paper. A more general extension could involve combining the methods introduced here with the ideas of Bressloff [10] regarding pattern formation on inhomogeneous domains. It would also be interesting to see if the results found here could be extended to a two layer system using one population of excitatory neurons and one of inhibitory neurons with appropriate nonnegative coupling weights [25, 35, 54].

We have concentrated only on the instability of circularly symmetric bumps with respect to perturbations that break that symmetry. There are many other pattern-forming mechanisms that can potentially be studied using the ideas presented here. One example is spiral wave formation [4, 50], a phenomenon that cannot occur in one-dimensional domains. We have observed these patterns in a system of the form (3.1) with purely positive (excitatory) coupling and a simple form of adaptation like that used in [41] to prevent the whole domain from becoming active (not shown).

Another extension would be to use the ideas presented here to study a network of spiking neurons to see whether the appearance of the sorts of patterns investigated here could be predicted in such a network. The firing rate function f would have to be the appropriate function for the neurons used, but provided the neurons do not synchronize, the profiles of

firing frequency as a function of space should be the same for the rate and spiking models [40], and the techniques presented here should be applicable.

In conclusion, the main result presented here is the link between PIDEs and PDEs. The techniques introduced here enable one to apply the results for pattern formation in PDEs (of which there are many [15, 21, 23, 24, 36, 48, 49, 51]) to systems involving spatial integrals [5, 6, 7, 8, 10, 12, 13, 16, 27, 28, 47, 53, 54, 55] for which there are far fewer results, but which are of great interest.

Appendix A. Symmetry properties of the two-dimensional Fourier transform. We define the two-dimensional Fourier transform of a function $g(x, y)$ to be

$$(A.1) \qquad F(g) \equiv \frac{1}{2\pi} \int_{-\infty}^{\infty} \int_{-\infty}^{\infty} e^{-i(\alpha x + \beta y)} g(x, y) dx\, dy.$$

Move to polar coordinates with $x = r \cos\theta$, $y = r \sin\theta$, $\alpha = \eta \cos\psi$, and $\beta = \eta \sin\psi$, and assume that g is a function of r only. Then (A.1) becomes

$$(A.2) \qquad F(g) = \frac{1}{2\pi} \int_{0}^{\infty} g(r) r \left[\int_{0}^{2\pi} e^{-ir\eta \cos(\theta - \psi)} d\theta \right] dr.$$

It is clear that the inner integral (and therefore $F(g)$) is independent of ψ, so we set $\psi = \pi/2$, and the inner integral in (A.2) becomes

$$(A.3) \qquad \int_{0}^{2\pi} e^{-ir\eta \sin\theta} d\theta.$$

Letting $z = e^{i\theta}$ and moving to the complex plane, we have

$$(A.4) \qquad \int_{0}^{2\pi} e^{-ir\eta \sin\theta} d\theta = \int_{C} \frac{e^{-r\eta(z - 1/z)/2}}{iz} dz,$$

where C is the unit circle in the complex plane. In [56, p. 161], it is shown that

$$(A.5) \qquad e^{\tau(z - 1/z)/2} = \sum_{N=-\infty}^{\infty} J_N(\tau) z^N,$$

where $J_N(\cdot)$ is the Bessel function of the first kind of order N. Thus, setting $\tau = -r\eta$, we have

$$(A.6) \qquad \int_{0}^{2\pi} e^{-ir\eta \sin\theta} d\theta = \sum_{N=-\infty}^{\infty} J_0(-r\eta) \int_{C} \frac{z^{N-1}}{i} dz = 2\pi J_0(-r\eta),$$

and using the evenness of J_0, (A.2) becomes

$$(A.7) \qquad F(g) = \int_{0}^{\infty} g(r) J_0(r\eta) r\, dr.$$

This is clearly a function of η $(= \sqrt{\alpha^2 + \beta^2})$ only.

Appendix B. A particular Fourier transform. We now show that

$$
(B.1) \qquad I \equiv \int_0^\infty e^{-kr} J_0(r\eta) r \, dr = \frac{k}{(k^2 + \eta^2)^{3/2}},
$$

which, in combination with (A.7), gives (3.25). We start with the series expansion of the Bessel function

$$
(B.2) \qquad J_0(x) = \sum_{n=0}^\infty \frac{(-1)^n x^{2n}}{2^{2n}(n!)^2}.
$$

Using this,

$$
(B.3) \qquad I = \sum_{n=0}^\infty \frac{(-1)^n \eta^{2n}}{2^{2n}(n!)^2} \int_0^\infty e^{-kr} r^{2n+1} dr = \sum_{n=0}^\infty \frac{(-1)^n \eta^{2n}(2n+1)!}{2^{2n}(n!)^2 k^{2n+2}},
$$

where the integral has been evaluated using the Gamma function. Now, using the notation $(a)_n = a(a+1)(a+2)\cdots(a+n-1)$ and the identity $(2n+1)! = 2^{2n} n! (3/2)_n$, we have

$$
(B.4) \quad I = \sum_{n=0}^\infty \frac{(-1)^n \eta^{2n}(3/2)_n}{n! \, k^{2n+2}} = \frac{1}{k^2} \sum_{n=0}^\infty \frac{(3/2)_n}{n!} \left(\frac{-\eta^2}{k^2}\right)^n = \frac{(1+\eta^2/k^2)^{-3/2}}{k^2} = \frac{k}{(k^2+\eta^2)^{3/2}}
$$

as was claimed in (B.1).

REFERENCES

[1] S. AMARI, *Homogeneous nets of neuron-like elements*, Biol. Cybernet., 17 (1975), pp. 211–220.

[2] S. AMARI, *Dynamics of pattern formation in lateral-inhibition type neural fields*, Biol. Cybernet., 27 (1977), pp. 77–87.

[3] S. AMARI, *Mathematical Theory of Neural Networks*, Sangyo-Tosho Publishers, Tokyo, 1978.

[4] D. BARKLEY, *Euclidian symmetry and the dynamics of rotating spiral waves*, Phys. Rev. Lett., 72 (1994), pp. 164–167.

[5] P. BATES AND F. CHEN, *Spectral analysis and multidimensional stability of traveling waves for non–local Allen–Cahn equation*, J. Math. Anal. Appl., 273 (2002), pp. 45–57.

[6] P. BATES, X. CHEN, AND A. CHMAJ, *Traveling Waves for Bistable Equations with Nonlocalities*, preprint, 2002.

[7] P. BATES, P. FIFE, X. REN, AND X. WANG, *Travelling waves in a convolution model for phase transitions*, Arch. Ration. Mech. Anal., 138 (1997), pp. 105–136.

[8] P. BATES AND X. REN, *Heteroclinic orbits for a higher order phase transition problem*, European J. Appl. Math., 8 (1997), pp. 149–163.

[9] W. H. BOSKING, Y. ZHANG, B. SCHOFIELD, AND D. FITZPATRICK, *Orientation selectivity and the arrangement of horizontal connections in tree shrew striate cortex*, J. Neurosci., 17 (1997), pp. 2112–2127.

[10] P. C. BRESSLOFF, *Traveling fronts and wave propagation failure in an inhomogeneous neural network*, Phys. D, 155 (2001), pp. 83–100.

[11] P. C. BRESSLOFF, *Bloch waves, periodic feature maps, and cortical pattern formation*, Phys. Rev. Lett., 89 (2002), 088101.

[12] P. C. BRESSLOFF AND J. D. COWAN, *The visual cortex as a crystal*, Phys. D, 173 (2002), pp. 226–258.

[13] P. C. BRESSLOFF, J. D. COWAN, M. GOLUBITSKY, P. J. THOMAS, AND M. WIENER, *Geometric visual hallucinations, Euclidean symmetry and the functional architecture of striate cortex*, Phil. Trans. Roy. Soc. B, 40 (2001), pp. 299–330.

[14] A. R. CHAMPNEYS, *Homoclinic orbits in reversible systems and their applications in mechanics, fluids and optics*, Phys. D, 112 (1998), pp. 158–186.

[15] X. CHEN AND M. KOWALCZYK, *Dynamics of an interior spike in the Gierer–Meinhardt system*, SIAM J. Math. Anal., 33 (2001), pp. 172–193.

[16] A. J. J. CHMAJ AND X. REN, *Pattern formation in the nonlocal bistable equation*, Methods Appl. Anal., 8 (2001), pp. 369–386.

[17] C. L. COLBY, J. R. DUHAMEL, AND M. E. GOLDBERG, *Oculocentric spatial representation in parietal cortex*, Cereb. Cortex, 5 (1995), pp. 470–481.

[18] A. COMPTE, N. BRUNEL, P. GOLDMAN-RAKIC, AND X.-J. WANG, *Synaptic mechanisms and network dynamics underlying spatial working memory in a cortical network model*, Cereb. Cortex, 10 (2000), pp. 910–923.

[19] S. COOMBES, G. LORD, AND M. OWEN, *Waves and bumps in neuronal networks with axo-dendritic synaptic interactions*, Phys. D, 178 (2003), pp. 219–241.

[20] J. M. SOTO-CRESPO, D. R. HEATLEY, E. M. WRIGHT, AND N. N. AKHMEDIEV, *Stability of higher-bound states in a saturable self-focusing medium*, Phys. Rev. A, 44 (1991), pp. 636–644.

[21] J. DOCKERY AND R. J. FIELD, *Numerical evidence of stationary and breathing concentration patterns in the Oregonator with equal diffusivities*, Phys. Rev. E, 58 (1998), pp. 823–832.

[22] E. DOEDEL, A. R. CHAMPNEYS, T. F. FAIRGRIEVE, Y. A. KUTZNETSOV, B. SANDSTEDE, AND X. WANG, *AUTO97: Continuation and Bifurcation Software for Ordinary Differential Equations (with HOMCONT)*, Tech. report, Concordia University, Montreal, Canada, 1997.

[23] A. DOELMAN, T. KAPER, AND P. ZEGELING, *Pattern formation in the one-dimensional Gray-Scott model*, Nonlinearity, 10 (1997), pp. 523–563.

[24] A. DOELMAN AND H. VAN DER PLOEG, *Homoclinic stripe patterns*, SIAM J. Appl. Dyn. Syst., 1 (2002), pp. 65–104.

[25] M. ENCULESCU AND M. BESTEHORN, *Activity dynamics in nonlocal interacting neural fields*, Phys. Rev. E, 67 (2003), 041904.

[26] G. B. ERMENTROUT, *Neural networks as spatio-temporal pattern forming systems*, Rep. Progr. Phys., 61 (1998), pp. 353–430.

[27] P. FIFE, *Clines and material interfaces with nonlocal interaction*, in Nonlinear Problems in Applied Mathematics, T. S. Angell, L. P. Cook, R. E. Kleinman, and W. E. Olmstead, eds., SIAM, Philadelphia, 1996, pp. 134–149.

[28] P. C. FIFE, *Pattern formation in gradient systems*, in Handbook for Dynamical Systems, Vol. 2, Applications, B. Fiedler, ed., North–Holland, Amsterdam, 2002, pp. 677–722.

[29] S. FUNAHASHI, C. J. BRUCE, AND P. S. GOLDMAN-RAKIC, *Mnemonic coding of visual space in the monkey's dorsolateral prefrontal cortex*, J. Neurophysiol., 61 (1989), pp. 331–349.

[30] B. GIDAS, W. M. NI, AND L. NIRENBERG, *Symmetry of positive solutions of elliptic equations in* R^N, in Mathematical Analysis and Applications, Part A, Adv. in Math. Suppl. Stud. 7a, Academic Press, New York, 1981, pp. 369–402.

[31] M. A. GIESE, *Dynamic Neural Field Theory for Motion Perception*, Kluwer Academic Publishers, Boston, 1998.

[32] D. GOLOMB AND Y. AMITAI, *Propagating neuronal discharges in neocortical slices: Computational and experimental study*, J. Neurophysiol., 78 (1997), pp. 1199–1211.

[33] Y. GUO, *Existence and Stability of Standing Pulses in Neural Networks*, Ph.D. thesis, University of Pittsburgh, Pittsburgh, PA, 2003.

[34] B. GUTKIN, G. B. ERMENTROUT, AND J. O'SULLIVAN, *Layer 3 patchy recurrent connections may determine the spatial organization of sustained activity in the primate frontal cortex*, Neurocomputing, 32–33 (2000), pp. 391–400.

[35] B. S. GUTKIN, C. R. LAING, C. C. CHOW, G. B. ERMENTROUT, AND C. L. COLBY, *Turning on and off with excitation: The role of spike–timing asynchrony and synchrony in sustained neural activity*, J. Comput. Neurosci., 11 (2001), pp. 121–134.

[36] J. K. HALE, L. A. PELETIER, AND W. C. TROY, *Exact homoclinic and heteroclinic solutions of the Gray–Scott model for autocatalysis*, SIAM J. Appl. Math., 61 (2000), pp. 102–130.

[37] D. HANSEL AND H. SOMPOLINSKY, *Modeling feature selectivity in local cortical circuits*, in Methods in Neuronal Modeling, 2nd ed., C. Koch and I. Segev, eds., MIT Press, Cambridge, MA, 1998.

[38] G. W. HUNT, M. A. PELETIER, A. R. CHAMPNEYS, P. D. WOODS, M. AHMER WADEE, C. J. BUDD, AND G. L. LORD, *Cellular buckling in long structures*, Nonlinear Dynam., 21 (2000), pp. 3–29.

[39] K. KISHIMOTO AND S. AMARI, *Existence and stability of local excitations in homogeneous fields*, J. Math. Biol., 7 (1979), pp. 303–318.

[40] C. R. LAING AND C. C. CHOW, *Stationary bumps in networks of spiking neurons*, Neural Comp., 13 (2001), pp. 1473–1494.

[41] C. R. LAING AND A. LONGTIN, *Noise–induced stabilization of bumps in systems with long–range spatial coupling*, Phys. D, 160 (2001), pp. 149–172.

[42] C. R. LAING AND W. C. TROY, *Two bump solutions of Amari–type models of working memory*, Phys. D, 178 (2003), pp. 190–218.

[43] C. R. LAING, W. C. TROY, B. GUTKIN, AND G. B. ERMENTROUT, *Multiple bumps in a neuronal model of working memory*, SIAM J. Appl. Math., 63 (2002), pp. 62–97.

[44] J. B. LEVITT, D. A. LEWIS, T. YOSHIOKA, AND J. S. LUND, *Topography of pyramidal neuron intrinsic connections in Macaque monkey prefrontal cortex (areas 9 and 46)*, J. Comp. Neurol., 338 (1993), pp. 360–376.

[45] E. K. MILLER, C. A. ERICKSON, AND R. DESIMONE, *Neural mechanisms of visual working memory in prefrontal cortex of the Macaque*, J. Neurosci., 16 (1996), pp. 5154–5167.

[46] D. MORGAN AND T. KAPER, *Axisymmetric ring solutions of the 2-D Gray Scott model and their destabilization into spots*, Phys. D, submitted.

[47] C. B. MURATOV, *Theory of domain patterns in systems with long-range interactions of Coulomb type*, Phys. Rev. E, 66 (2002), 066108.

[48] C. B. MURATOV AND V. V. OSIPOV, *General theory of instabilities for patterns with sharp interfaces in reaction-diffusion systems*, Phys. Rev. E, 53 (1996), pp. 3101–3116.

[49] C. B. MURATOV AND V. V. OSIPOV, *Stability of the static spike autosolitons in the Gray–Scott model*, SIAM J. Appl. Math., 62 (2002), pp. 1463–1487.

[50] J. D. MURRAY, *Mathematical Biology*, 2nd ed., Springer–Verlag, Berlin, 1993.

[51] Y. NISHIURA AND D. UEYAMA, *A skeleton structure for self-replicating patterns*, Phys. D, 130 (1999), pp. 73–104.

[52] L. A. PELETIER AND W. C. TROY, *Patterns: Higher Order Models in Physics and Chemistry*, Birkhäuser Boston, Boston, 2001.

[53] D. J. PINTO AND G. B. ERMENTROUT, *Spatially structured activity in synaptically coupled neuronal networks: I. Traveling fronts and pulses*, SIAM J. Appl. Math., 62 (2001), pp. 206–225.

[54] D. J. PINTO AND G. B. ERMENTROUT, *Spatially structured activity in synaptically coupled neuronal networks: II. Lateral inhibition and standing pulses*, SIAM J. Appl. Math., 62 (2001), pp. 226–243.

[55] S. RUUTH, B. MERRIMAN, AND S. OSHER, *Convolution generated motion as a link between cellular automata and continuum pattern dynamics*, J. Comput. Phys., 151 (1999), pp. 836–861.

[56] M. R. SPIEGEL, *Complex Variables with an Introduction to Conformal Mapping*, Schaum's Outline Series, McGraw-Hill, New York, 1998.

[57] J. SERRIN, *A symmetry problem in potential theory*, Arch. Ration. Mech. Anal., 43 (1971), pp. 304–318.

[58] S. M. STRINGER, T. P. TRAPPENBERG, E. T. ROLLS, AND I. E. T. DE ARAUJO, *Self-organizing continuous attractor networks and path integration: One-dimensional models of head direction cells*, Network-Comp. Neural, 13 (2002), pp. 217–242.

[59] J. G. TAYLOR, *Neural "bubble" dynamics in two dimensions: Foundations*, Biol. Cybernet., 80 (1999), pp. 393–409.

[60] E. THELEN, G. SCHONER, C. SCHEIER, AND L. SMITH, *The dynamics of embodiment: A field theory of infant perseverative reaching*, Behavioral and Brain Sciences, 24 (2001), pp. 1–34.

[61] L. N. TREFETHEN, *Spectral Methods in MATLAB*, Software Environ. Tools 10, SIAM, Philadelphia, 2000.

[62] M. USHER, M. STEMMLER, AND Z. OLAMI, *Dynamic pattern formation leads to $1/f$ noise in neural populations*, Phys. Rev. Lett., 74 (1995), pp. 326–329.

[63] X. J. Wang, *Synaptic reverberation underlying mnemonic persistent activity*, Trends Neurosci., 24 (2001), pp. 455–463.

[64] T. Wennekers, *Dynamic approximation of spatio–temporal receptive fields in nonlinear neural field models*, Neural Computation, 14 (2002), pp. 1801–1825.

[65] H. Werner and T. Richter, *Circular stationary solutions in two-dimensional neural fields*, Biol. Cybernet., 85 (2001), pp. 211–217.

[66] H. R. Wilson and J. D. Cowan, *A mathematical theory of the functional dynamics of cortical and thalamic nervous tissue*, Kybernetic, 13 (1973) pp. 55–80.

[67] K. Zhang, *Representation of spatial orientation by the intrinsic dynamics of the head–direction cell ensemble: A theory*, J. Neurosci., 16 (1996), pp. 2112–2126.